Urchin-like TiO$_2$ structures decorated with lanthanide-doped Bi$_2$S$_3$ quantum dots to boost hydrogen photogeneration performance

Magdalena Miodyńska[a], Alicja Mikolajczyk[a,b], Beata Bajorowicz[a], Julia Zwara[a], Tomasz Klimczuk[c], Wojciech Lisowski[d], Grzegorz Trykowski[e], Henry P. Pinto[f], Adriana Zaleska-Medynska[a,*]

[a] Department of Environmental Technology, Faculty of Chemistry, University of Gdansk, 80-308, Gdansk, Poland
[b] Laboratory of Environmental Chemometrics, University of Gdansk, 80-308, Gdansk, Poland
[c] Department of Solid State Physics, Faculty of Applied Physics and Mathematics, Gdansk University of Technology, 80-233, Gdansk, Poland
[d] Institute of Physical Chemistry, Polish Academy of Science, 01-224, Warsaw, Poland
[e] Faculty of Chemistry, Nicolaus Copernicus University, 87-100, Torun, Poland
[f] CompNano Group, School of Physical Sciences and Nanotechnology, Yachay Tech University, 100119, Urcuqui, Ecuador

ARTICLE INFO

ABSTRACT

The formation of heterojunctions between wide- and narrow-bandgap photocatalysts is commonly employed to boost the efficiency of photocatalytic hydrogen generation. Herein, the photoactivity of urchin-like rutile particles is increased by decorating with pristine as well as Er- or Yb-doped Bi$_2$S$_3$ quantum dots (QDs) at varied QD loadings (1–20 wt%) and doping degrees (1–15 mol%), and the best hydrogen evolution performance is achieved at Er and Yb contents of 10 mol%. Specifically, a hydrogen productivity of 1576.7 µmol g$_{cat}^{-1}$ is achieved after 20-h irradiation for TiO$_2$ decorated by 10 mol% Yb-doped Bi$_2$S$_3$ QDs. Theoretical calculations show that the introduction of defects into the Bi$_2$S$_3$ lattice through Er/Yb doping promotes the creation of new energy levels and facilitates the transport of photogenerated charges during photocatalysis.

1. Introduction

Heterogeneous photocatalysis is one of the most promising methods of obtaining molecular hydrogen, a prospective future energy carrier, additionally allowing for the decomposition of contaminants in liquid and gas phases [1–6] To date, the upscaling of heterogeneous photocatalytic processes is mainly hindered by their low efficiency, especially in the case of hydrogen generation. Hence, much effort has been made to find ways of circumventing this problem, as exemplified by the modification of wide-bandgap (wide-BG) semiconductor matrices with narrow-BG quantum dots (QDs) to simultaneously enhance efficiency and utilise visible (as opposed to ultraviolet (UV)) light. QDs are semiconductor nanocrystals with sizes of 2–10 nm that experience the quantum confinement effect [7,8] and hence feature unique properties not observed for their macro- or micro-counterparts [9]. For example, the size-dependent optical properties of QDs allow for broadband radiation absorption, especially in the visible-light region. Furthermore, as the extremely high *surface*-to-volume ratio of QDs can be used to promote photocatalytic reactions at the catalyst surface [7], QDs have been explored as photocatalytic reaction promoters.

Among the broad range of QDs, those comprising Cd and Pb compounds such as CdS, CdO, CdSe, CdTe, and PbS are used most often because of their advantageous conduction and valence band edge positions as well as the narrow BG and ease of synthesis [10–13]. In particular, these QDs have been used for visible light–induced pollutant degradation [14–20] and photocatalytic hydrogen generation [21–26]. Unfortunately, the toxicity of Pb-/Cd- based QDs limits their practical applications, especially those associated with environmental remediation [27,28], which necessitates the search for less harmful and more stable QDs. To date, diverse QDs have been synthesised, characterised, and evaluated in terms of photoactivity, as exemplified by carbon [29–32], AgBr [33], ZnO [34], graphene [35], black P [36], InP [37], MoS$_2$ [38], CuInS$_2$ [39,40], CeO$_2$ [41], In$_2$S$_3$ [42], CuO [43], Cu$_2$O [44], Ag$_3$PO$_4$ [45], Bi$_2$WO$_6$ [46], BiVO$_4$ [47], SnS [48], Ag$_2$S [49], and Bi$_2$S$_3$ [44,50,51] QDs, which have been used for the photocatalytic degradation of organic pollutants and/or hydrogen production via photocatalytic water splitting. In most cases, QDs are deposited at the surface of three-dimensional semiconductor structures to create photoactive composites, as this hybridisation allows one to hinder the rapid recombination of photogenerated charges observed for pristine QDs and

---

thus increase the efficiency of QD usage in photocatalytic reactions [7].

Herein, Bi_2S_3 QDs were selected because of their appropriate conduction band (CB) edge position (sufficient for the reduction of protons to molecular hydrogen during the photocatalytic process) and narrow BG (1.3–1.7 eV) [52]. Previous works revealed that the introduction of rare earth (RE) ions into a foreign crystal lattice creates additional electronic states to indirectly promote both near-infrared (NIR) radiation absorption and emission in the visible or UV range [53,54]. In this case, an effective conversion of visible and NIR light energy can afford UV light (via the so-called upconversion), which can then excite broadband semiconductors [55]. Hence, the introduction of RE ions (Er^{3+} and Yb^{3+}) into the crystal lattice of Bi_2S_3 QDs was expected to increase the photocatalytic activity of the resulting RE-Bi_2S_3 QD/TiO_2 hybrids. Previous research largely focused on the doping of TiO_2 with lanthanides [56–59] and confirmed the resulting photoactivity increase; however, lanthanide doping has also been shown to increase the photoactivity of CdS, ZnS, and ZnO QDs [8,60]. To the best of our knowledge, only one paper has dealt with the doping of Bi_2S_3 with lanthanides, describing the modification of flower-like Bi_2S_3 with Eu ions and the application of the resulting hybrids for pollutant photodegradation [61].

In contrast, Bi_2S_3 QD–decorated rutile hybrids have not been applied to hydrogen evolution; moreover, Er- and Yb-doped Bi_2S_3 QDs (and hence, their composites) have not even been synthesised. In view of the above, the present study probes the effect of Bi_2S_3 QD loading onto urchin-like rutile particles as well as the influence of Er and Yb doping on the photoactivity of doped-Bi_2S_3 QD/TiO_2 composites, providing experimental and theoretical evidence concerning the mechanism of hydrogen evolution over as-prepared hybrids. The above-mentioned composites with well dispersed Bi_2S_3 QDs (pristine and Er- or Yb-doped) at the surface of urchin-like rutile particles are synthesised by a combination of solvothermal and direct adsorption methods, and the hydrogen evolution performances of these composites are evaluated in electrolytes containing Na_2S/Na_2SO_3 or triethanolamine (TEOA) as a sacrificial agent under UV–vis and visible-light (> 420 nm) irradiation. Furthermore, density functional theory (DFT) calculations are applied to assess the effects of RE ion introduction into the crystal structure of Bi_2S_3. The usefulness of our contribution lies in the development of Cd-free QDs and in the deepening of our understanding of the interactions between Bi_2S_3-based QDs and the rutile matrix and related reagents during hydrogen evolution.

The formation of RE-Bi_2S_3/TiO_2 hybrids is confirmed by structural (powder X-ray diffraction, pXRD) and surface (X-ray photoelectron spectroscopy, XPS) analyses, and the obtained samples are shown to exhibit higher photocatalytic activity for the water splitting reaction than their individual components (Bi_2S_3 QDs and rutile TiO_2). Computer simulations of Bi_2S_3 QDs doped with Yb^{3+} and Er^{3+} are used to determine the resulting changes in Bi_2S_3 crystal lattice and, in combination with experiments, help to elucidate the photocatalytic mechanism. The highest activity is observed for the composite containing 10 mol% Yb-doped Bi_2S_3 QDs at a loading of 10 wt%, in which case hydrogen productivity after 4 h reaches 376.4 $\mu mol\ g_{cat}^{-1}$. This enhanced activity is ascribed to (i) the introduction of Yb^{3+} into the interstitial space of QDs to reduce the BG to 0.4 eV, as indicated by theoretical studies; (ii) the use of an optimal sulphur-containing electrolyte to stabilise the exposure system; and (iii) the facilitated transport of photogenerated charges due to the creation of an effective TiO_2-Bi_2O_3-RE-doped Bi_2S_3 semiconductor connection via surface oxidation of Bi_2S_3 during thermal treatment in the last step of composite synthesis.

2. Experimental

2.1. Materials and instruments

Ti(IV) butoxide (TBOT; Sigma-Aldrich) and concentrated HCl (35–38%, STANLAB) were used for the preparation of TiO_2 spheres. Pristine and RE-doped Bi_2S_3 QDs were prepared from $Bi(NO_3)_3 \cdot 5\ H_2O$ (analytical grade, STANLAB), $Na_2S_2O_3 \cdot 5\ H_2O$ (pure, POCH S.A.), Er $(NO_3)_3 \cdot 5\ H_2O$ (99.99%, Sigma-Aldrich), $Yb(NO_3)_3 \cdot 5\ H_2O$ (99.99%, Sigma-Aldrich), and acetone (STANLAB). Deionised water and ethanol (96 vol%, POCH S.A.) were used to purify the obtained photocatalysts. The electrolytes used for photocatalytic measurements were prepared from $Na_2S \cdot 9\ H_2O$ (analytical grade, EUROCHEM BGD), Na_2SO_3 (analytical grade, POCH S.A.), NaOH (analytical grade, STANLAB), and TEOA ($C_6H_{15}NO_3$, > 99%, Carl Roth GmbH + Co. KG). All chemicals were used as received without further purification.

Diffuse reflectance spectra were recorded on a UV–vis spectrophotometer (UV 2600, Shimadzu) equipped with an integrating 4 sphere in the range of 200–800 nm using a $BaSO_4$ reference. Phase composition was probed by pXRD using a Bruker D8 Advance Eco diffractometer (Cu K_α) equipped with a LynxEye-XE detector. The collected data were analysed by the Le Bail method using HighScore Plus ver. 3.0e software. The morphology and size of TiO_2 particles and QDs were probed by field-emission scanning electron microscopy (FE-SEM; JEOL JSM-7610 F) and transmission electron microscopy (TEM; STEM-EDX, FEI Europe, TecnaiF20 X-Twin). Photoluminescence (PL) measurements were carried out at 20 °C using an LS-50B luminescence spectrophotometer equipped with a Xe discharge lamp as an excitation source and an R928 photomultiplier as a detector. Excitation radiation ($\lambda = 325$ nm) was directed on the sample surface at an angle of 90°. The elemental compositions of QD nanocomposite surfaces were evaluated by XPS (PHI 5000 VersaProbe, ULVAC-PHI) using monochromatic Al K_α radiation ($h\nu = 1486.6$ eV).

2.2. TiO_2 preparation

TiO_2 particles were hydrothermally prepared as described elsewhere [62]. Briefly, TBOT (68 g) was added to concentrated HCl (60 mL) upon stirring over 10 min, and the mixture was then transferred into a Teflon-lined stainless steel autoclave and heated at 170 °C for 24 h. The reactor was cooled to room temperature, and the TiO_2 precipitate was sequentially washed with water and ethanol for three times, dried at 70 °C until complete liquid evaporation, and calcined at 300 °C for 1 h.

2.3. Preparation of pristine and RE-doped Bi_2S_3 QDs

Bi_2S_3 QDs were synthesised using a refined solvothermal method [63]. Briefly, $Bi(NO_3)_3 \cdot 5\ H_2O$ was dissolved in acetone (140 mL) to a concentration of 4.77 mM upon vigorous stirring over 30 min. The solution was treated with $Na_2S_2O_3 \cdot 5\ H_2O$ (0.248 g), stirred for 30 min, and the obtained yellowish suspension was transferred into a Teflon-lined stainless steel autoclave and heated at 180 °C for 24 h. After cooling to room temperature, the dark brown powder of QDs was sequentially washed with water and ethanol (three times each, with centrifugation (6000 rpm) after each wash) and dried at 80 °C overnight. For the synthesis of RE-doped Bi_2S_3 QDs, Er or Yb nitrate was introduced at the stage of $Bi(NO_3)_3$ solution preparation. RE ions were assumed to be incorporated into the QD crystal structure instead of Bi; therefore, the extent of doping was expressed as mol% RE with respect to Bi, and the sum of Bi + RE nitrate amounts was held constant. In this way, Bi_2S_3 QDs doped with Er or Yb at levels of $x = 1, 5, 10,$ and 15 mol% were obtained (xRE_Bi_2S_3).

2.4. Combination of QDs with TiO_2

Composites with different amounts of QDs deposited on TiO_2 were prepared by a physical adsorption method. For this purpose, a beaker filled with doubly distilled water (25 mL) was charged with TiO_2 (1 g) and an appropriate amount of QDs (corresponding to loadings of 1, 3, 5, 10, 15, or 20 wt%) or 10RE_Bi_2S_3 powder and placed in an ultrasonic

bath for 10 min. The obtained suspension was magnetically stirred for 1 h and then evaporated to dryness at 70 °C overnight. For better QD anchoring on TiO_2, the composites were calcined at 300 °C for 1 h at a ramp rate of 5 °C min^{-1}. The photocatalyst exhibiting the highest activity for hydrogen evolution, namely $10Yb\_10Bi_2S_3/TiO_2$ was also calcined at 350 and 400 °C for 1 h.

2.5. Photocatalytic activity measurements

Typically, a cylindrical quartz reactor was charged with the photocatalyst (100 mg) and aqueous electrolyte (80 mL; 10 wt% TEOA or 0.1 M Na_2S/0.5 M Na_2SO_3/1 M NaOH) and tightly closed with a silicone septum. The suspension was stirred at 700 rpm and a constant temperature of 10 °C. For the first 30 min, the process was run without irradiation to establish an adsorption-desorption equilibrium between the photocatalyst and the solution, and the space above the suspension was purged with nitrogen. Then, a reference air sample from the suspension was collected by a syringe and analysed. The system was subsequently irradiated by a 1000-W Xe lamp (Oriel), and control air samples were collected every hour. The total exposure time was 4 h (or 20 h for the stability testing of the most photoactive composite). The hydrogen content of collected air samples was determined by a gas chromatograph equipped with a Thermal Conductivity Detector. For measurements of visible-light photocatalytic activity, a long-pass filter with a cut-off of 420 nm was employed.

2.6. Theoretical calculations

DFT calculations were performed using the plane-wave-basis Vienna *ab initio* simulation package (VASP) [64–66]. Core electrons were described by projected augmented wave potentials, with potentials for S, Bi, Er, and Yb atoms generated in $[Ne]3s^23p^4$, $[Xe, 4f^{14}]5d^{10}6s^26p^3$, $[Kr, 4d^{10}5s^24f^{11}]5p^66s^25d^1$, and $[Kr, 4d^{10}5s^24f^{14}]5p^66s^2$ electron configurations, respectively, where square brackets denote core electron configurations. The optimal bulk crystal structures of Bi_2S_3 and RE-Bi_2S_3 QDs were computed using the strongly constrained and appropriately normed (SCAN) meta-generalised gradient approximation [67,68] with long-range van der Waals interactions from the revised Vydrov–van Voorhis nonlocal correlation functional (SCAN + rVV10) [69]. The total energy was converged to < 1 meV atom^{-1} using a kinetic cut-off energy of 600 eV and an appropriate Γ-centred Monkhorst–Pack *k*-point mesh with a separation of 0.035 Å^{-1}. Finally, ionic optimisations were performed until all the forces were below 0.01 eV Å^{-1}. The electronic structure of RE-Bi_2S_3 was studied using a $1 \times 3 \times 1$ supercell considering the presence of either S or Bi vacancies as well as RE_S, RE_{Bi}, and RE_{int} sites. The band structure of pristine Bi_2S_3 was computed using the hybrid Hartree–Fock DFT functional (Heyd–Scuseria–Ernzerhof hybrid functional HSE12 [70]) using the optimal atomic structure obtained by SCAN + rVV10.

3. Results and discussion

To investigate the effect of QD loading and doping degree on photocatalyst properties, we prepared a range of RE-Bi_2S_3 QD/TiO_2 composites (Table 1) as well as bare TiO_2 and pristine Bi_2S_3 QDs as references.

3.1. Morphology

The shape and size of TiO_2 particles and (RE)-Bi_2S_3 QDs as well as the distribution of QDs on the TiO_2 surface were probed by SEM and TEM (Fig. 1). SEM imaging (Figs. 1a and b) revealed that TiO_2 particles were spherical (diameter = 6–7 μm) and comprised individual rods, thus resembling sea urchins. Fig. 1c presents a TEM image of a non-modified TiO_2 particle fragment, revealing that the constituent rods with a diameter of ~50 nm had a defect-free smooth surface. The size

Table 1
Compositions of the prepared photocatalysts.

Sample label	Loading of (RE)-Bi_2S_3 QDs on the TiO_2 matrix	Type and amount of dopant introduced into QDs
TiO_2	–	–
Bi_2S_3 QDs	–	–
$1Bi_2S_3/TiO_2$	1 wt%	–
$3Bi_2S_3/TiO_2$	3 wt%	–
$5Bi_2S_3/TiO_2$	5 wt%	–
$10Bi_2S_3/TiO_2$	10 wt%	–
$15Bi_2S_3/TiO_2$	15 wt%	–
$20Bi_2S_3/TiO_2$	20 wt%	–
$1Er\_10Bi_2S_3/TiO_2$	10 wt%	1 mol% Er
$5Er\_10Bi_2S_3/TiO_2$	10 wt%	5 mol% Er
$10Er\_10Bi_2S_3/TiO_2$	10 wt%	10 mol% Er
$15Er\_10Bi_2S_3/TiO_2$	10 wt%	15 mol% Er
$1Yb\_10Bi_2S_3/TiO_2$	10 wt%	1 mol% Yb
$5Yb\_10Bi_2S_3/TiO_2$	10 wt%	5 mol% Yb
$10Yb\_10Bi_2S_3/TiO_2$	10 wt%	10 mol% Yb
$15Yb\_10Bi_2S_3/TiO_2$	10 wt%	15 mol% Yb

distribution of spherical QDs was estimated by TEM imaging of bulk QDs (Fig. 1d) and composites (Fig. 1f–n). The main fraction (~73%) of QDs had diameters of 3–6 nm, while ~32% of QDs had diameters of 4–5 nm (see details in Fig. 1d). Fig. 1f–i indicates the homogenous distribution of QDs at the TiO_2 surface. Moreover, the increase in QD loading resulted in a higher surface density of QDs distributed at TiO_2 facets, which was particularly noticeable when the loading increased from 5 to 10 wt% (Fig. 1f–g). TEM imaging of hybrids containing Er- or Yb-doped Bi_2S_3 QDs (Figs. 1j–n) demonstrated that doping did not affect the shape, size, and surface distribution of Bi_2S_3 QDs. Sample elemental compositions were examined by TEM/EDX (Transmission Electron Microscope/Energy Dispersive X-Ray Analysis) (Fig. 1o) to confirm the presence of Er, while Yb was invisible at this characterisation stage.

Furthermore, during TEM analysis, it was possible to capture the moment of QD movement on the TiO_2 surface due to the interaction of matter with high-energy electrons from the electron beam (Video S1 in the Supplementary Information, SI). This movement was attributable to heating induced by electron beam focusing and vacuum conditions in the TEM chamber. A similar phenomenon was reported by Wang et al. for Bi_2S_3 nanorods [71].

3.2. Optical properties

The absorption and emission spectra of photocatalysts are presented in Fig. 2 and 3, respectively. Fig. 2a shows that whereas bare TiO_2 absorbed radiation with wavelengths of up to 400 nm, decoration with Bi_2S_3 QDs allowed the absorption range to be extended into the visible region. The BG of pristine TiO_2 was calculated as 3–3.1 eV from its absorption range and was in line with the formation of the rutile phase. The QD content of composites (1–20 wt%) was positively correlated with the intensity of visible-light ($\lambda > 400$ nm) absorbance. In contrast, no such correlation was observed between visible-light absorption intensity and the Er/Yb content of QDs (Fig. 2b).

Among Er-doped photocatalysts, the composite with 10 mol% Er-doped QDs featured the highest intensity of visible-light absorption and activity for photocatalytic hydrogen production (Fig. 9 and 10d). Similarly, among the synthesised QDs, those doped with 10 mol% Er showed the highest absorption intensity (Fig. 2c). However, no such trend was observed for Yb-containing samples, in which case the highest composite absorbance intensity was observed for $5Yb\_10Bi_2S_3/TiO_2$ (Fig. 2b), while among Yb-doped Bi_2S_3 QDs, the strongest absorbance was observed for those doped with 15 mol% Yb (Fig. 2d).

Fig. 3 presents photocatalyst PL spectra (excitation wavelength = 315 nm), revealing a correlation between the decrease in luminescence intensity (in relation to that of bare TiO_2) and the increase in the
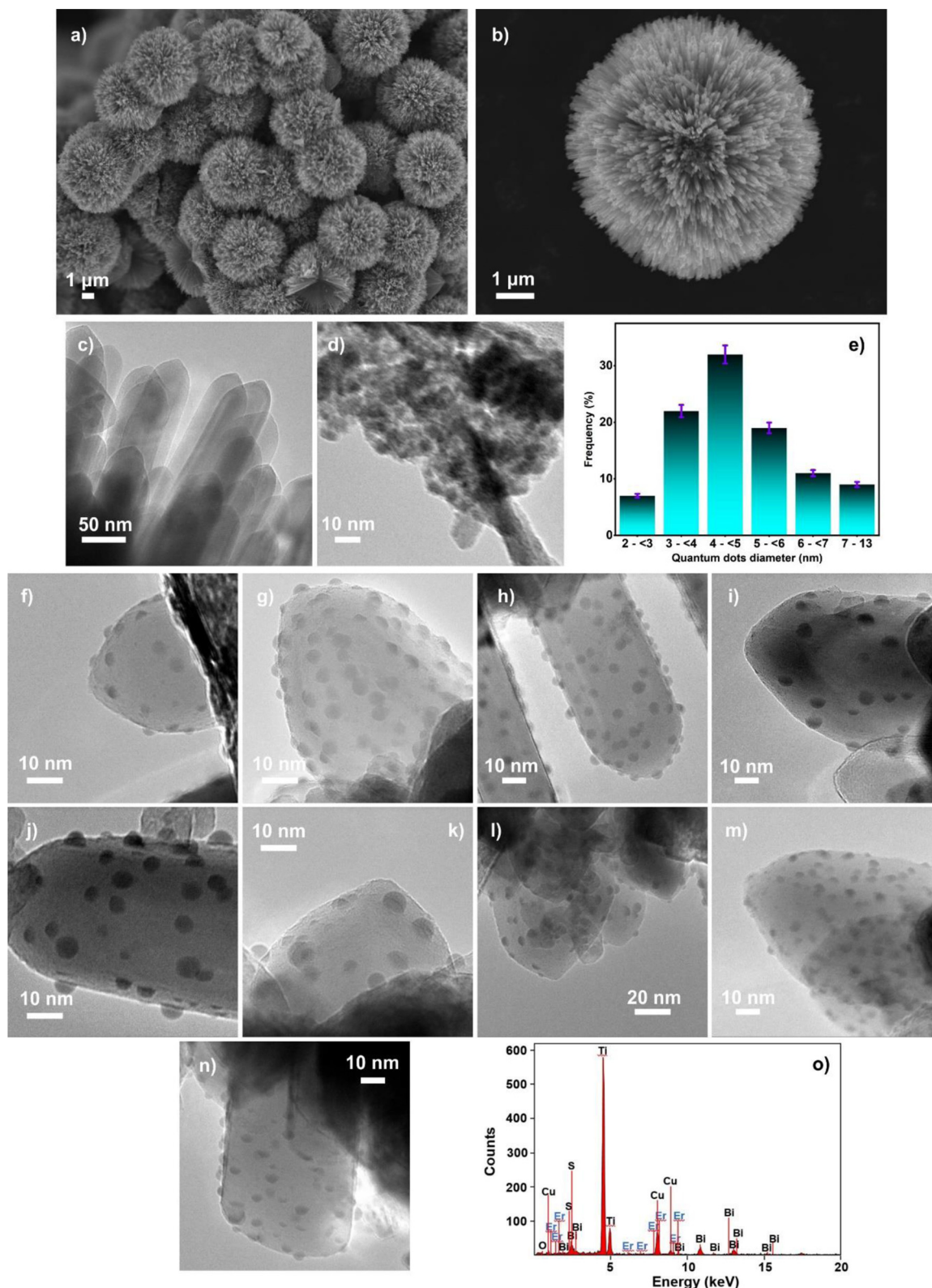
Fig. 1. SEM (a, b) and TEM (c) images of urchin-like TiO_2 structures. (d) TEM image of Bi_2S_3 QDs. (e) Size distribution of Bi_2S_3/$RE\_Bi_2S_3$ QDs. TEM images of (f) $5Bi_2S_3/TiO_2$, (g) $10Bi_2S_3/TiO_2$, (h) $15Bi_2S_3/TiO_2$, (i) $20Bi_2S_3/TiO_2$, (j) $1Er\_10Bi_2S_3/TiO_2$, (k) $5Er\_10Bi_2S_3/TiO_2$, (l) $10Er\_10Bi_2S_3/TiO_2$, (m) $5Yb\_10Bi_2S_3/TiO_2$, and (n) $10Yb\_10Bi_2S_3/TiO_2$. (o) EDX analysis of $10Er\_10Bi_2S_3/TiO_2$.

QD content of composites. A significant decrease in luminescence was also detected for composites containing RE-doped Bi_2S_3 QDs. The simultaneous decrease in luminescence and an increase in photocatalytic activity were ascribed to the inhibition of photogenerated charge

recombination [44,72]. Additionally, all PL spectra featured four characteristic emission bands of TiO_2 at 421, 449, 484, and 530 nm. The band at 421 nm was ascribed to the existence of self-trapped excitons from TiO_6^{8-} octahedra [73,74], while those at 449 and 484 nm
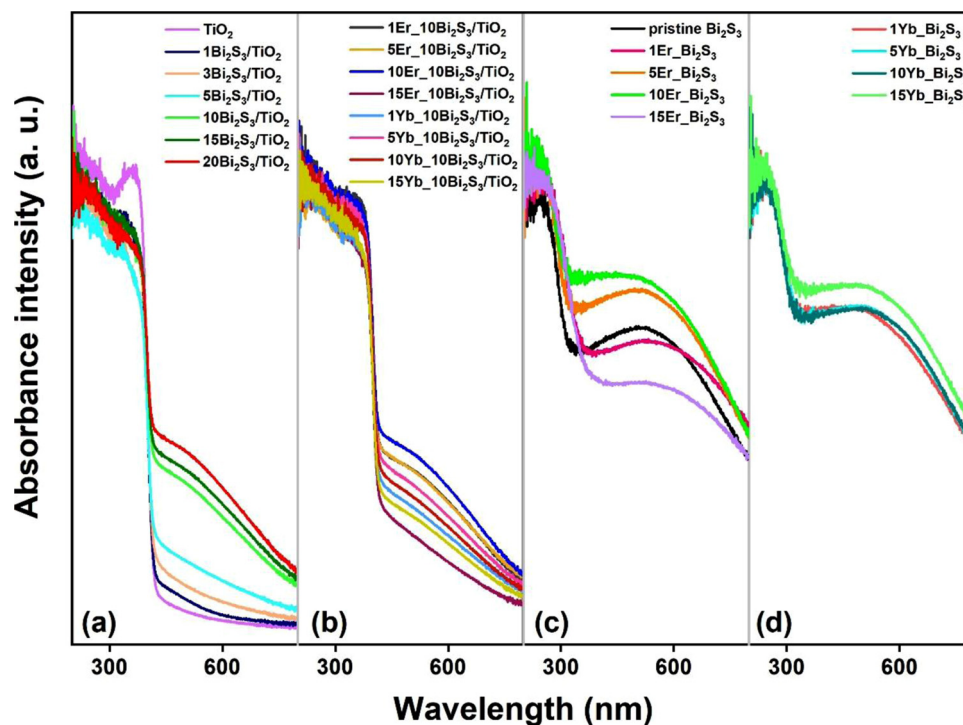
Fig. 2. UV–vis/diffuse reflectance spectra of the prepared photocatalysts: a) bare TiO_2 and Bi_2S_3/TiO_2 composites; b) RE-Bi_2S_3/TiO_2; c) Er-Bi_2S_3 QDs and d) Yb-Bi_2S_3 QDs.

were attributed to the presence of surface defects such as oxygen vacancies, which formed intermediate energy states below the CB and could therefore trap electrons. Finally, the peak at 530 nm was ascribed to the radiative recombination of charge carriers [73,75].

3.3. XPS

The surface elemental compositions of bare TiO_2 and QD/TiO_2 hybrids were probed by XPS (Table 2).

Because of the overlap between Bi 4d/Ti 2p and Bi 4f/S 2p spectra, Bi and Ti contents were evaluated using the combination of Bi $3p_{3/2}$

spectra and deconvoluted Bi 4d + Ti 2p and Bi 4f spectra. S content was determined from S 2 s spectra. An exemplary set of these spectra collected for $10Bi_2S_3/TiO_2$ is shown in Fig. 4a and b.

The Ti 2p spectrum of $10Bi_2S_3/TiO_2$ confirmed the presence of TiO_2 (Fig. 4a, main Ti $2p_{3/2}$ signal at 458.8 eV [68]). The dominant Bi $4f_{7/2}$ signal at 159.4 eV (Bi 4f + S 2p spectrum, Fig. 4a) evidenced the presence of Bi(+3) due to Bi_2S_3 deposition [76], while signals located at lower binding energies indicated the coexistence of Bi $(+3-x)$ and Bi (0) surface states [76,77], the contribution of which was relatively large for TiO_2 doped with 1–3 wt% Bi_2S_3 (Table 2 and Bi 4f spectra in Fig. 5).

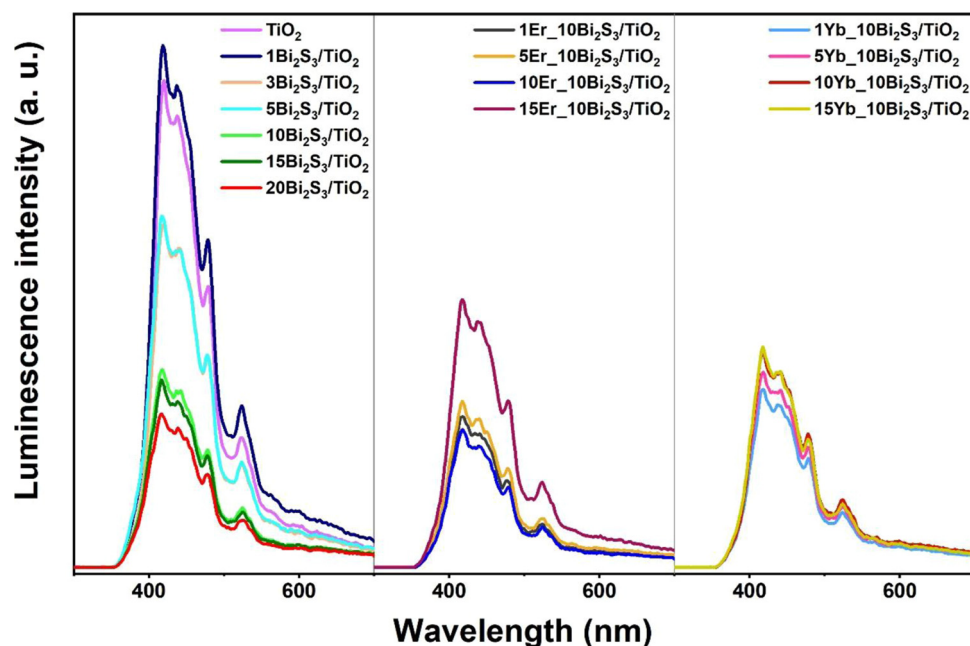The S 2 s spectrum of $10Bi_2S_3/TiO_2$ (Fig. 4b) was well fitted by two

Fig. 3. PL spectra of the prepared photocatalysts (λ_{ex} = 315 nm).

Table 2
Elemental contents and Bi valence states in the surface layer of QD/TiO$_2$ samples.

Sample	Ti (at%)	Bi[a] (at%)	Fraction of Bi4f$_{7/2}$ state (%)			O (at%)	S (at%)	Other (C N Cl) (at%)
			Bi(0) 156.7 eV	Bi($+3-x$) 157.5 $\pm$ 0.2 eV	Bi($+3$) 159.4 $\pm$ 0.2 eV			
TiO$_2$	24.9	0	0	0	0	65.7	0	9.4
Bi$_2$S$_3$ QDs	0	17.3	0	17.2	82.8	48.1	12.4	22.2
1Bi$_2$S$_3$/TiO$_2$	24.4	0.1	60.3	11.2	28.5	67.2	0.3	8.0
3Bi$_2$S$_3$/TiO$_2$	22.8	1.1	19.7	36.9	43.4	65.0	1.1	10.0
5Bi$_2$S$_3$/TiO$_2$	17.9	5.6	0	11.2	88.8	61.6	1.8	13.1
10Bi$_2$S$_3$/TiO$_2$	14.3	8.3	0	13.9	86.1	62.8	4.3	10.3
15Bi$_2$S$_3$/TiO$_2$	11.4	10.5	0	10.2	89.8	62.1	5.4	10.6
20Bi$_2$S$_3$/TiO$_2$	9.1	12.1	0	4.1	95.9	63.9	5.8	9.1

[a] Average values determined from Bi 4p$_{3/2}$ and Bi 4d/Bi 4f deconvoluted X-ray photoelectron spectra.
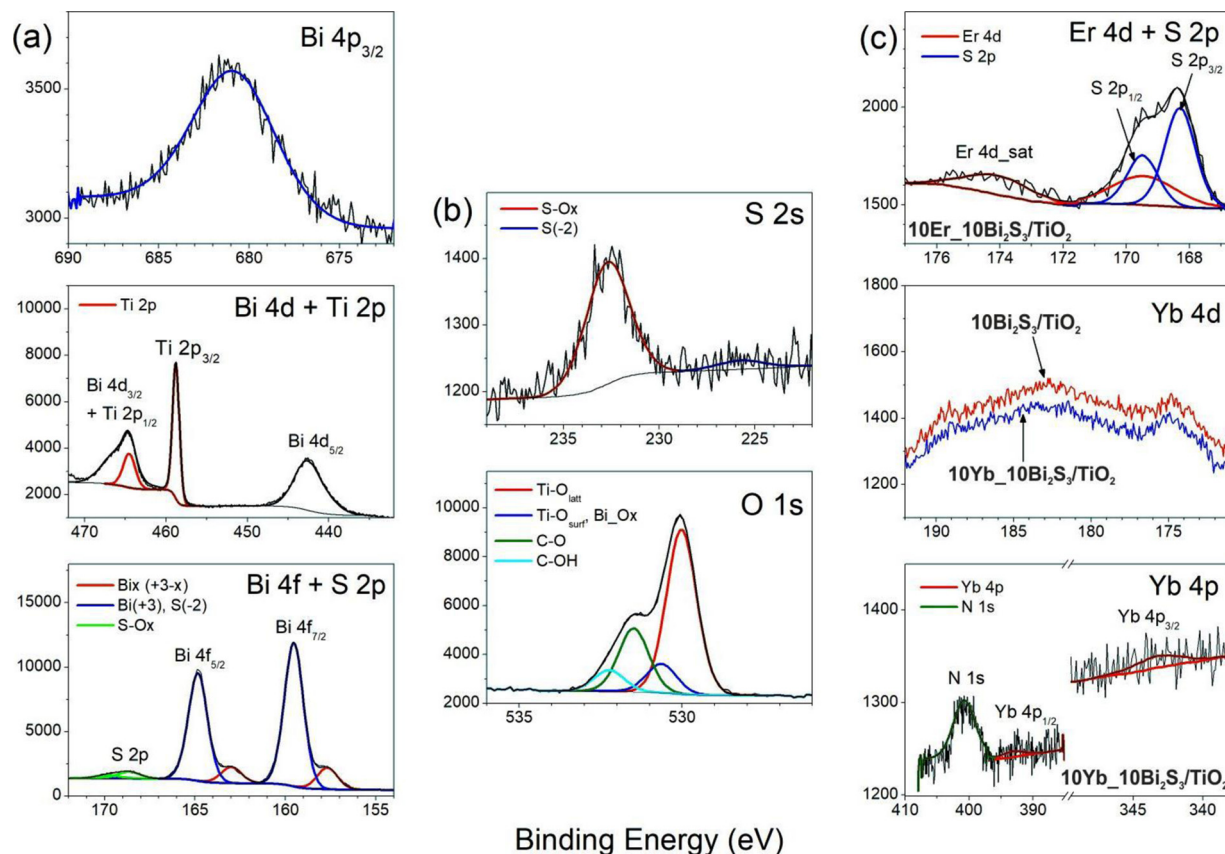

Fig. 4. High-resolution X-ray photoelectron spectra of 10Bi$_2$S$_3$/TiO$_2$: (a) Bi 4p$_{3/2}$, Bi 4d + Ti 2p, Bi 4f + S 2p; (b) S 2s, O 1s. (c) X-ray photoelectron spectra of doped elements: Er 4d overlapping with S 2p, Yb 4d, and Yb 4p.

peaks at 232.4 and 225.2 eV, attributed to surface sulphates and sulphides, respectively [76,77].

The presence of Er and Yb at the surface of RE-doped Bi$_2$S$_3$ QDs was confirmed by analysis of Er 4d and Yb 4d core level spectra, with representative spectra collected for 10Er_10Bi$_2$S$_3$/TiO$_2$ and 10Yb_10Bi$_2$S$_3$/TiO$_2$ presented in Fig. 4c. Unfortunately, Er 3d spectra overlapped with S 2p ones, while Yb 4d signals were too weak to be detected because of the overlap with relatively strong plasmonic Bi 4f signals (see Yb 4d region in the spectra of 10Bi$_2$S$_3$/TiO$_2$ and 10Yb_10Bi$_2$S$_3$/TiO$_2$). However, the effective doping of Er($+3$) was confirmed by observation of Er 4d and Er 4d satellite signals at 169.4 and 174.0 eV, respectively [78,79]. The presence of Yb was confirmed by analysis of high-resolution Yb 4p spectra (Fig. 4c). Despite the very low signal/noise ratio, two signals at 343.2 and 393.2 eV, attributable to Yb 4p$_{3/2}$ and Yb 4p$_{1/2}$, respectively, could be distinguished [76]. However, the suitability of these spectra for Yb content evaluation was doubtful. In fact, the amounts of Er and Yb species at the surface of all

RE-doped samples were much smaller that nominal values (Table 3).

10Yb_10Bi$_2$S$_3$/TiO$_2$ exhibited the highest photocatalytic activity, and its pristine-state surface chemical composition was therefore compared with that obtained after photocatalytic processing in different electrolytes (0.1 M Na$_2$S/0.5 M Na$_2$SO$_3$/1 M NaOH and 10 wt% TEOA). The corresponding XPS data are presented in Table 3 and Fig. 6, with 10Yb_10Bi$_2$S$_3$/TiO$_2$_20h_TEOA and 10Yb_10Bi$_2$S$_3$/TiO$_2$_20h_ES denoting samples subjected to prolonged irradiation (20 h) in TEOA and Na$_2$S/Na$_2$SO$_3$ electrolytes, respectively.

The Bi 4f spectrum recorded for the sample processed in TEOA (Fig. 6) revealed a much smaller content of Bi($+3$) species than that of the sample processed in the Na$_2$S/Na$_2$SO$_3$ electrolyte. Moreover, the surface content of Bi significantly decreased after photocatalytic processing in TEOA solution (Table 3), which indicated the advanced decomposition of Yb-doped Bi$_2$S$_3$ QDs. In contrast, this process was inhibited when 0.1 M Na$_2$S/0.5 M Na$_2$SO$_3$/1 M NaOH was used as an electrolyte.

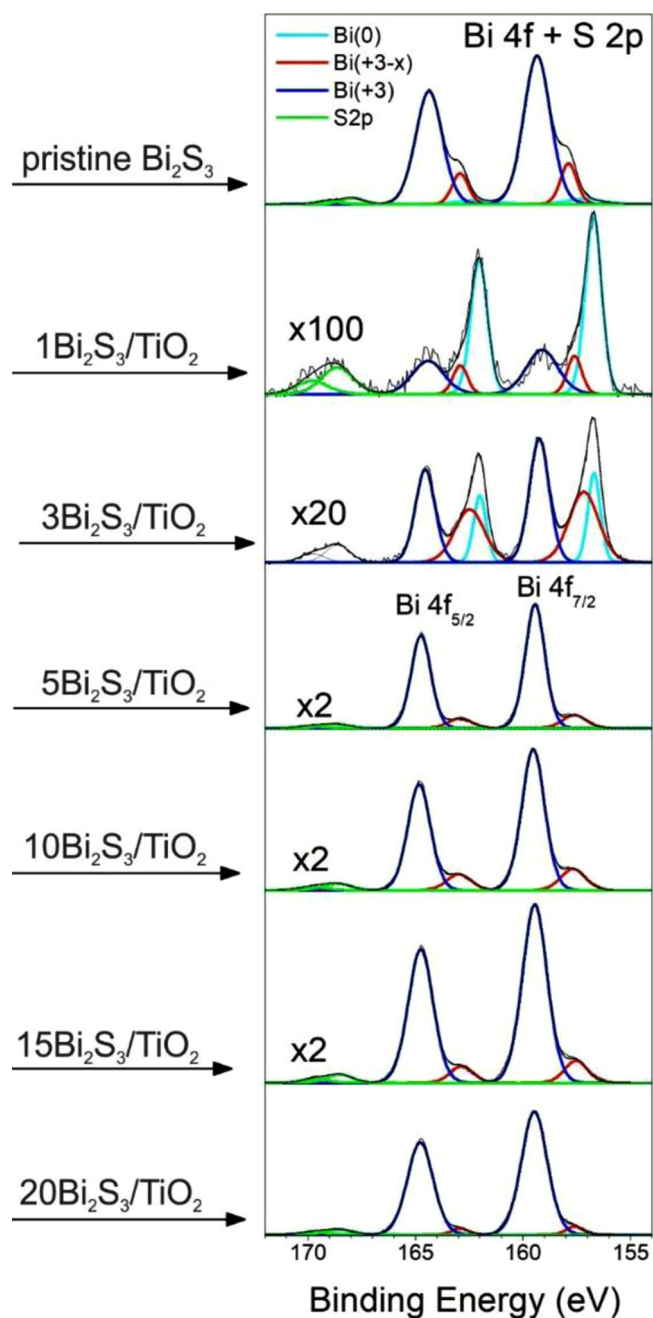**Fig. 5.** Bi 4f X-ray photoelectron spectra of Bi_2S_3/TiO_2 samples with different Bi_2S_3 contents.

3.4. XRD

Fig. 7 presents the powder X-ray diffraction (pXRD) patterns of bare TiO_2, Bi_2S_3 QDs, and selected composites. In the case of bare TiO_2, all signals originated from TiO_2 (rutile), with the strongest peak at $2\theta = 27°$ corresponding to reflection from the (110) plane. We also provide the Miller indices for the strongest peaks. The peaks expected for TiO_2 are shown by black vertical bars. Contrary to that of TiO_2, the pattern of Bi_2S_3 QDs featured weak peaks barely discernible from the amorphous-like background. The pXRD pattern with a broad maximum at around 30° is similar to reported in ref. [80–82]. The low intensity reflections can be indexed by an orthorhombic Bi_2S_3 phase (red vertical bars) [83], but Le Bail analysis was not performed. Notably, the above pattern contained no peaks of $Bi(NO_3)_3$ or $Na_2S_2O_3$.

In the pattern of $10Bi_2S_3/TiO_2$ (Fig. 7c), the strongest reflections

were attributable to the rutile phase, whereas weak peaks marked by arrows probably indicated the presence of Bi_2O_3 (monoclinic P21/c) phase. Doping with 10 mol% Er or Yb had no influence on pXRD patterns.

The Le Bail method was used to estimate the lattice parameters of the rutile structure (P42/mnm), affording values of $a = 4.5955(1)$ Å and $c = 2.9581(1)$ Å for bare TiO_2, which were very close to those ($a = 4.5924$ Å and $c = 2.9575$ Å) reported in ref. [84]. The lattice parameters of composites differed from those of the pristine sample by less than 0.03%, i.e., were essentially the same.

In contrast to XPS, pXRD did not confirm the presence of Bi_2S_3 and instead might suggested the presence of Bi_2O_3 in composites. As no Er and Yb oxides were detected (Figs. 7d and e), this may finding indirectly supported the hypothesis that Er and Yb ions substituted other ions in the QD phase.

Furthermore, the composite with the highest photoactivity, $10Yb\_10Bi_2S_3/TiO_2$, was probed by pXRD after a 20-h photocatalytic process in TEOA and sulphide/sulphite electrolytes (Fig. 8). The pattern recorded after irradiation in the TEOA electrolyte indicated the absence of Bi-based QDs, as opposed to that of the pristine sample (Fig. 8c), demonstrating the destructive effect of the reaction environment during photocatalysis. This effect was also observed in the images of samples and electrolytes before and after photocatalysis (Fig. 11).

The pXRD pattern recorded after irradiation in the sulphide/sulphite electrolyte (Fig. 8b) featured weak peaks (marked by arrows) that could not be indexed to monoclinic Bi_2O_3 and were instead ascribed to the cubic (I23 s.g. #197) phases of γ-Bi_2O_3 ($a = 10.267$ Å) and $NaBi_{12}O_{18.5}$ ($a = 10.2635$ Å). However, more detailed crystallographic studies are required to characterise the unknown phase.

3.5. Photocatalytic activity

The performances of as-prepared samples for photocatalytic water splitting are presented in Fig. 9 and 10. Specifically, Fig. 9 shows the time course of hydrogen generation under UV–vis irradiation in the presence of the sulphide/sulphite electrolyte. First, the effect of QD loading was assessed, and the highest activity was observed at a loading of 10 wt%. In particular, 4-h irradiation resulted in the formation of 239.9 and 296.7 μmol hydrogen g_{cat}^{-1} in the presence of non-modified and 10 wt%-QD-decorated TiO_2, respectively. Thus, the effects of QD doping by Er/Yb were further investigated for hybrids with a QD loading of 10 wt% (Fig. 9). The highest hydrogen productivity was observed in the presence of $10Yb\_10Bi_2S_3/TiO_2$. Moreover, doping with both Er and Yb at 10 mol% benefitted hydrogen production, with hydrogen yields of 376.4 and 339 μmol g_{cat}^{-1} observed after 4-h irradiation for $10Yb\_10Bi_2S_3/TiO_2$ and $10Er\_10Bi_2S_3/TiO_2$ samples, respectively. Interestingly, pristine Bi_2S_3 QDs featured a low hydrogen generation activity (72.4 μmol g_{cat}^{-1} after 4 h), probably due to the rapid recombination of photogenerated electron-hole pairs therein.

The most active composite ($10Yb\_10Bi_2S_3/TiO_2$) was selected to investigate the effect of calcination temperature on photocatalytic activity. For this investigation, an additional batch of this composite was synthesised, divided into three parts in the final preparation stage, and annealed at 300, 350 or 400 °C for 1 h. Photocatalytic activity measurements revealed that the initially chosen calcination temperature (300 °C) was optimal, while a temperature increase to 400 °C resulted in decreased photoactivity (Fig. 10a). This photoactivity loss was ascribed to the complete oxidation of Bi_2S_3 to Bi_2O_3 at ≥ 350 °C, as reported previously [85]. The CB edge of Bi_2O_3 is more positive (+0.33 eV [86]) than that of Bi_2S_3 (−0.76 eV [86]), and the reduction potential of the former is too low to reduce hydrogen, which results in the suppression of hydrogen evolution in the presence of a Bi_2O_3-containing composite. Thus, we concluded that photocatalyst annealing at 300 °C causes the surface oxidation of Bi_2S_3 to Bi_2O_3 (confirmed by XPS analysis and described in section 3.3), while annealing at higher temperatures leads to complete oxidation. Consequently, the presence of both sulphide and

Table 3
Contents and valence states of elements in the surface layer of RE-doped Bi_2S_3/TiO_2 samples.

| Sample	Ti (at%)	Bi (at%)	Fraction of $Bi4f_{7/2}$ state (%)			O (at%)	S (at%)	Er (at%)	Yb (at%)	Other (C N Cl) (at%)
			Bi(0) $156.4 \pm 0.2\,eV$	Bi($+3-x$) $157.6 \pm 0.1\,eV$	Bi($+3$) $159.4 \pm 0.2\,eV$					
$10Bi_2S_3/TiO_2$	14.3	8.3	0	13.9	86.1	62.8	4.3	0	0	10.3
$1Er\_10Bi_2S_3/TiO_2$	14.1	7.1	0	12.0	88.0	62.1	4.7	0.5	0	11.5
$5Er\_10Bi_2S_3/TiO_2$	13.1	8.1	0	6.7	93.3	62.3	4.8	0.5	0	11.2
$10Er\_10Bi_2S_3/TiO_2$	14.3	7.0	0	9.8	90.1	64.1	4.8	0.7	0	9.1
$15Er\_10Bi_2S_3/TiO_2$	14.5	7.3	0	4.9	95.1	64.9	4.1	0.8	0	8.4
$1Yb\_10Bi_2S_3/TiO_2$	14.1	10.2	0	10.9	89.1	61.7	3.7	0	0.1	10.3
$5Yb\_10Bi_2S_3/TiO_2$	13.9	10.3	0	7.4	92.6	63.1	4.1	0	0.1	8.5
$10Yb\_10Bi_2S_3/TiO_2$	14.0	10.1	0	6.2	93.8	60.3	4.4	0	0.1	11.1
$15Yb\_10Bi_2S_3/TiO_2$	14.3	9.9	0	16.2	83.8	62.2	3.8	0	0.1	9.7
$10Er\_Bi_2S_3$ QDs	0	22.3	3.6	14.1	82.3	42.0	14.8	0.6	0	20.3
$10Yb\_Bi_2S_3$ QDs	0	23.9	2.3	10.8	86.9	46.0	12.4	0	0.2	17.5
$10Yb\_10Bi_2S_3/TiO_2\_20h\_TEOA$	21.5	1.8	54.7	13.8	31.5	59.2	0.4	0	0.1	17.0
$10Yb\_10Bi_2S_3/TiO_2\_20h\_ES$	19.2	5.9	23.2	9.4	67.4	64.1	1.1	0	0.1	9.6
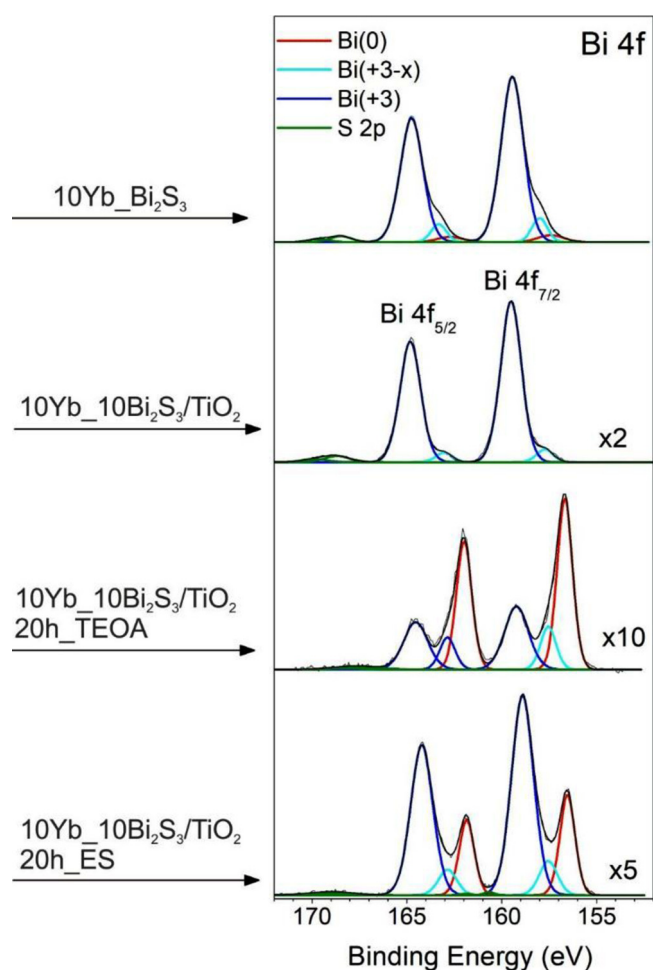
Fig. 6. Bi 4f X-ray photoelectron spectra of $10Yb\_10Bi_2S_3/TiO_2$ before and after photocatalytic processing in 0.1 M Na_2S/0.5 M Na_2SO_3/1 M NaOH and 10 wt% TEOA. The corresponding Bi 4f spectrum for $10Yb\_10Bi_2S_3$ QDs without the TiO_2 matrix is shown for comparison.

Fig. 7. pXRD patterns of (a) bare TiO_2, (b) Bi_2S_3 QDs, (c) $10Bi_2S_3/TiO_2$, (d) $10Er\_10Bi_2S_3/TiO_2$, and (e) $10Yb\_10Bi_2S_3/TiO_2$. Vertical bars show the expected peak positions for rutile TiO_2 (black) and Bi_2S_3 (red). Arrows in (c–e) indicate peaks of monoclinic Bi_2O_3. The depicted lattice parameters of rutile TiO_2 were estimated by the Le Bail method. (For interpretation of the references to colour in this figure legend, the reader is referred to the web version of this article.)

oxide phases in QDs could improve the transport of photogenerated charges. Moreover, Bi_2S_3 facilitated hydrogen generation because of the appropriate position of the Bi_2S_3 CB edge, while the exclusive presence of Bi_2O_3 was undesirable. The reaction mechanism involving such a composite is comprehensively described in section 3.7.

Blank experiments indicated that a certain amount of hydrogen is generated in the absence of photocatalysts via direct photolysis of the
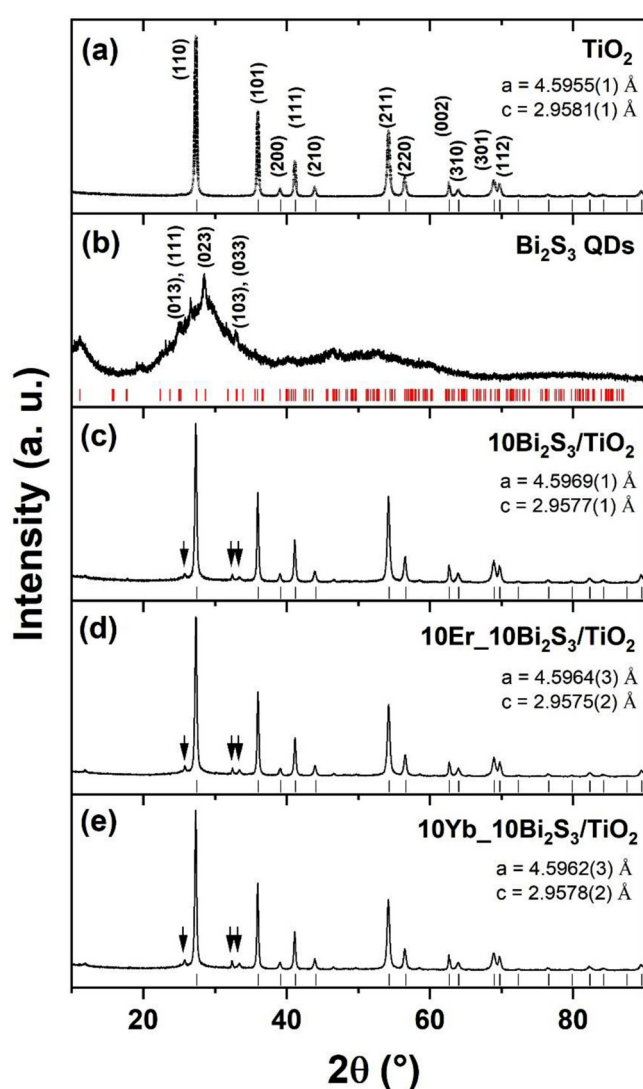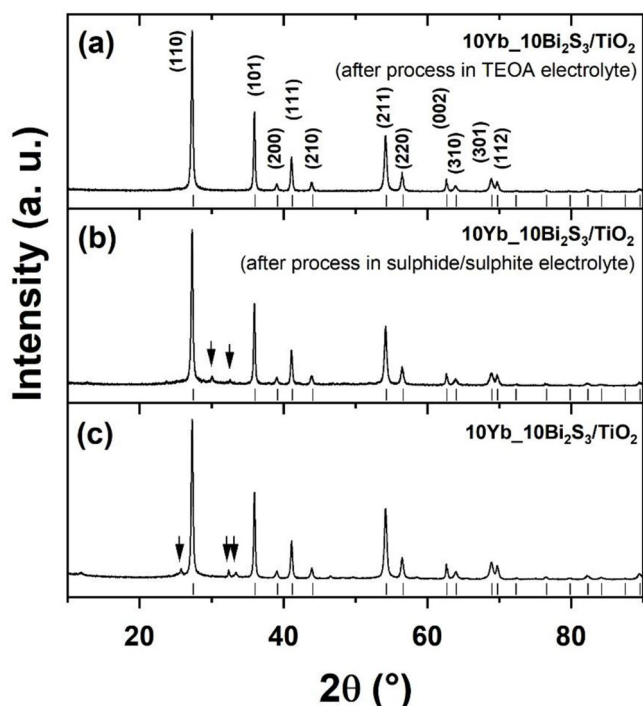
Fig. 8. pXRD patterns of (c) pristine 10Yb_10Bi$_2$S$_3$/TiO$_2$ and the same composite after the photocatalytic process in (a) TEOA and (b) sulphide/sulphite electrolytes. Arrows in (b) and (c) indicate the peaks of an unknown phase and monoclinic Bi$_2$O$_3$, respectively.

Na$_2$S/Na$_2$SO$_3$ electrolyte [87], as discussed in detail in section 3.7. To minimise the effect of sacrificial agent hydrolysis, we used 10 wt% aqueous triethanolamine (TEOA) as an appropriate sacrificial agent for sulphide and oxide-based photocatalysts. However, no hydrogen evolution was previously observed during TEOA irradiation in the absence of a photocatalyst [87]. The efficiencies of hydrogen generation in the presence of Na$_2$S/Na$_2$SO$_3$ and TEOA with and without photocatalysts

over 4 and 20 h are presented in Fig. 10. The results obtained for the TEOA electrolyte were consistent with those reported previously [87] and confirmed that hydrogen is not generated during irradiation in the absence of a photocatalyst. On the other hand, H$_2$ was generated when the Yb-doped Bi$_2$S$_3$ QD/rutile composite was introduced into this system, although the hydrogen yield dropped from 376.4–72.2 μmol g$_{cat}^{-1}$ when TEOA was used as a sacrificial agent instead of Na$_2$S/Na$_2$SO$_3$. Catalyst stability was probed by a long-term (20-h) hydrogen evolution test in the presence of the most active sample (10Yb_10Bi$_2$S$_3$/TiO$_2$) and both sacrificial agents (Fig. 10c). As a result, hydrogen was constantly produced in the presence of both Na$_2$S/Na$_2$SO$_3$ and TEOA, although the yield observed after 20-h irradiation in the former case (1576.7 μmol g$_{cat}^{-1}$) was much higher than that in the latter case (264.2 μmol g$_{cat}^{-1}$). After these tests, the spent photocatalyst was collected and characterised by XPS and XRD. Both techniques revealed the destructive effect of TEOA on the Yb-Bi$_2$S$_3$ QD/TiO$_2$ photocatalyst (see detailed discussion in section 3.3 and 3.4). On the other hand, the catalyst was stable during irradiation in the sulphide/sulphite electrolyte. Furthermore, XRD analysis indicated the incorporation of sodium derived from the sulphide/sulphite electrolyte (1 M NaOH) and the creation of a new crystalline phase, which could not be matched to any pattern of crystallographic databases (Fig. 8b). The available literature presents some reports on the photocatalytic activity increase of various photocatalysts [88–90]. Fig. 11 shows images of 10Yb_10Bi$_2$S$_3$/TiO$_2$ before and after processing in two different electrolytes and the colours of these electrolytes before and after processing. Notably, the originally colourless TEOA electrolyte became yellow-brown after the photocatalytic process, while the photocatalyst powder simultaneously turned from brown-yellow to light yellow. This behaviour suggested the dissolution of brown Bi$_2$S$_3$ QDs in the electrolyte during irradiation. In contrast, the sulphide/sulphite electrolyte remained colourless after 20-h irradiation, even though the photocatalyst became darker, probably because of sodium incorporation.

Finally, all photocatalysts were tested for hydrogen evolution activity in the sulphide/sulphite electrolyte under visible-light irradiation. Notably, hydrogen production after 4-h irradiation was observed only for three samples, but hydrogen yields were much lower than those observed in UV–vis tests (Fig. 10d). Thus, only 10Bi$_2$S$_3$/TiO$_2$,
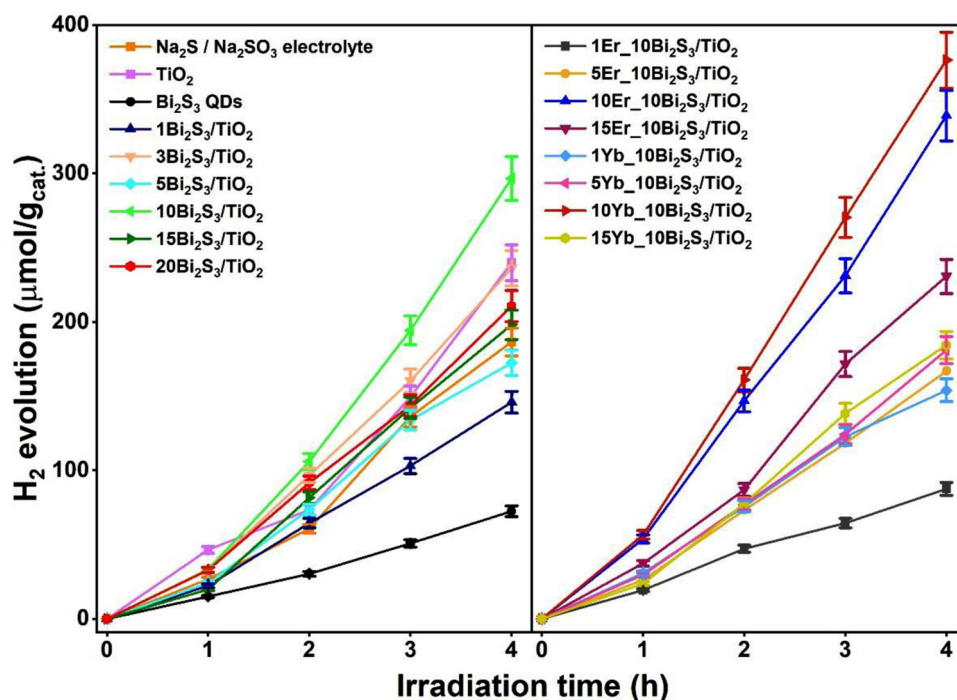

Fig. 9. Profiles of photocatalytic hydrogen evolution under UV–vis irradiation.

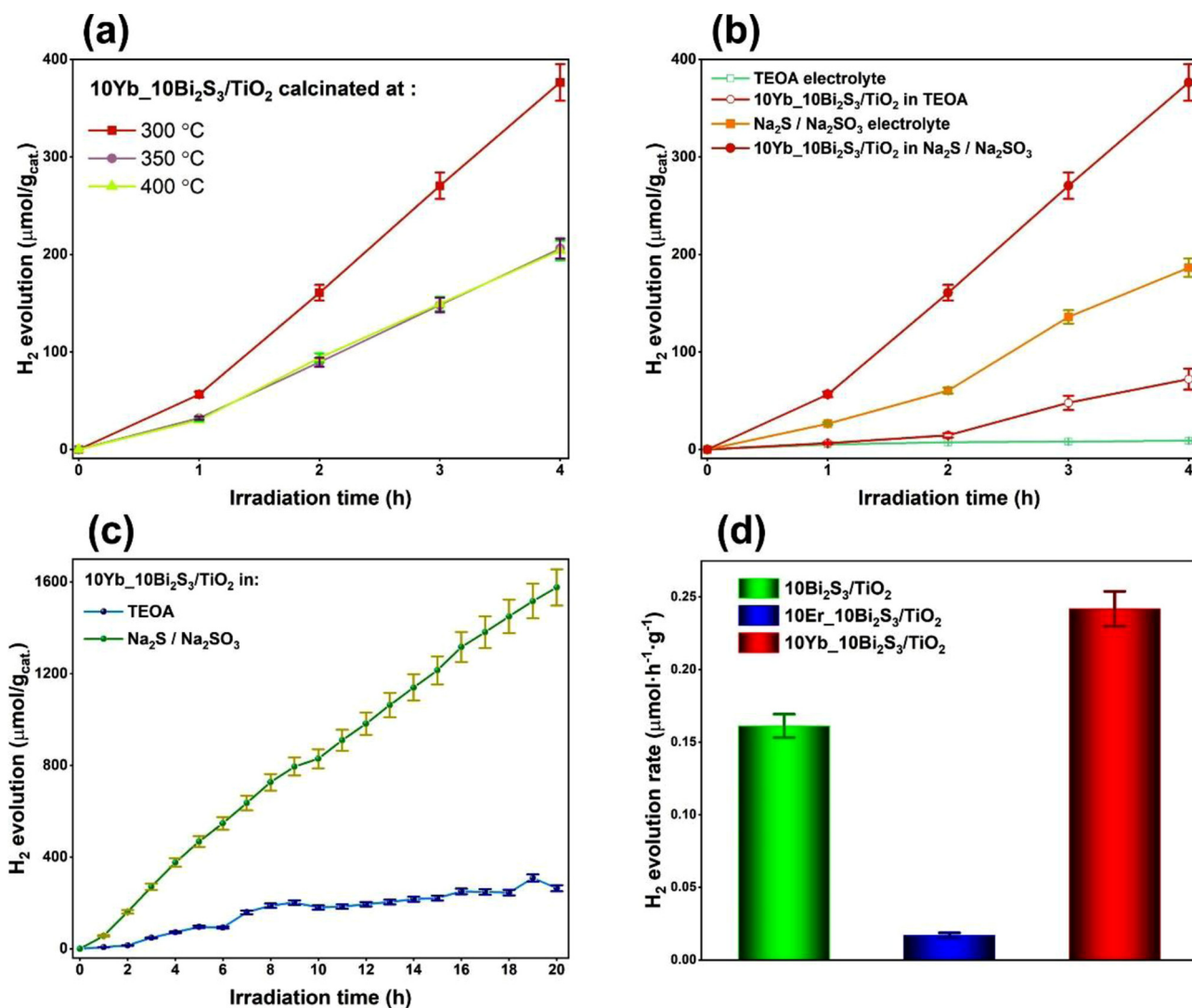**Fig. 10.** Photocatalytic hydrogen evolution (a) under UV–vis irradiation in the sulphide/sulphite electrolyte in the presence of 10Yb_10Bi$_2$S$_3$/TiO$_2$ calcined at different temperatures; (b) under UV–vis irradiation in the presence of 10Yb_10Bi$_2$S$_3$/TiO$_2$ in two different electrolytes; (c) under long-term UV–vis irradiation in the presence of 10Yb_10Bi$_2$S$_3$/TiO$_2$ in two different electrolytes; (d) under 4-h visible-light irradiation in the presence of 10Yb_10Bi$_2$S$_3$/TiO$_2$ in the sulphide/sulphite electrolyte.

10Er_10Bi$_2$S$_3$/TiO$_2$, and 10Yb_10Bi$_2$S$_3$/TiO$_2$ samples featured measurable visible light–induced photoactivity. A reference test revealed that no hydrogen was produced in the sulphur-based electrolyte under visible-light irradiation in the absence of a photocatalyst.

3.6. Theoretical calculations

The effect of doping on the photocatalytic activity of RE-Bi$_2$S$_3$ QDs was probed by DFT-based electronic structure calculations. Pristine Bi$_2$S$_3$ has an orthorhombic structure that belongs to the *Pbnm* space group (symmetry No. 62), with its crystals having a layered structure across the *a* lattice vector (Fig. 12 and Table 4). The crystal structure and physical properties of Bi$_2$S$_3$ computed by SCAN + rVV10 are presented in Table 4.

The band structure of pristine Bi$_2$S$_3$ was computed using both SCAN + rVV10 and hybrid HSE12 functionals. The simulations suggested a system with an indirect BG of 1.4 eV (1.98 eV for HSE12) (cf. Fig. 13), in good agreement with experimental data [91]. Furthermore, according to the computed partial density of states (PDOS), the upper valence band comprised S 2p states with a small contribution of Bi 6 s and Bi 6p states, while the lower CB comprised Bi 6p and S 2p states (Fig. 13b).

The SCAN + rVV10-computed PDOS for defects in a (1 × 3 × 1) Bi$_2$S$_3$ supercell with V$_S$ and V$_{Bi}$ vacancies (Fig. 14a) are displayed in Fig. 14b and Table 5. V$_S$ defects showed the formation of a defective level within the BG that features contributions of S 2p and Bi 6p states, while V$_{Bi}$ defects showed the formation of a hole state above the VB (cf. Fig. 14b).

The electronic properties of RE-Bi$_2$S$_3$ QDs were simulated using a 1 × 3 × 1 supercell of Bi$_2$S$_3$ containing 60 atoms (i.e., 24 Bi atoms and 36 S atoms), which corresponds to an RE content of ∼33 mg per gram Bi$_2$S$_3$. Within this supercell, we first investigated the formation of S and Bi vacancies (V$_S$ and V$_{Bi}$, respectively) and then, based on the obtained results, considered RE doping on V$_S$(3) (RE$_S$) and V$_{Bi}$(2) (RE$_{Bi}$) sites as well as RE interstitials (RE$_{int}$). The crystal symmetry of Bi$_2$S$_3$ suggests that it has three S and two Bi non-equivalent sites, as displayed in Fig. 14a. DFT calculations were performed for each vacancy type (V$_S$ and V$_{Bi}$), with the computed formation energies of neutral defects listed in Table 5. The most stable vacancy formation site for S (Bi) was identified as V$_S$(3), with the corresponding formation energy equalling 4.66 eV [7.36 eV for V$_{Bi}$(2)] (cf. Fig. 14a, Table 5.

Then, we investigated the doping of RE on V$_S$(3) and V$_{Bi}$(2) sites and the computed formation energies of different configurations, with results listed in Table 5. In addition, we also considered RE interstitials
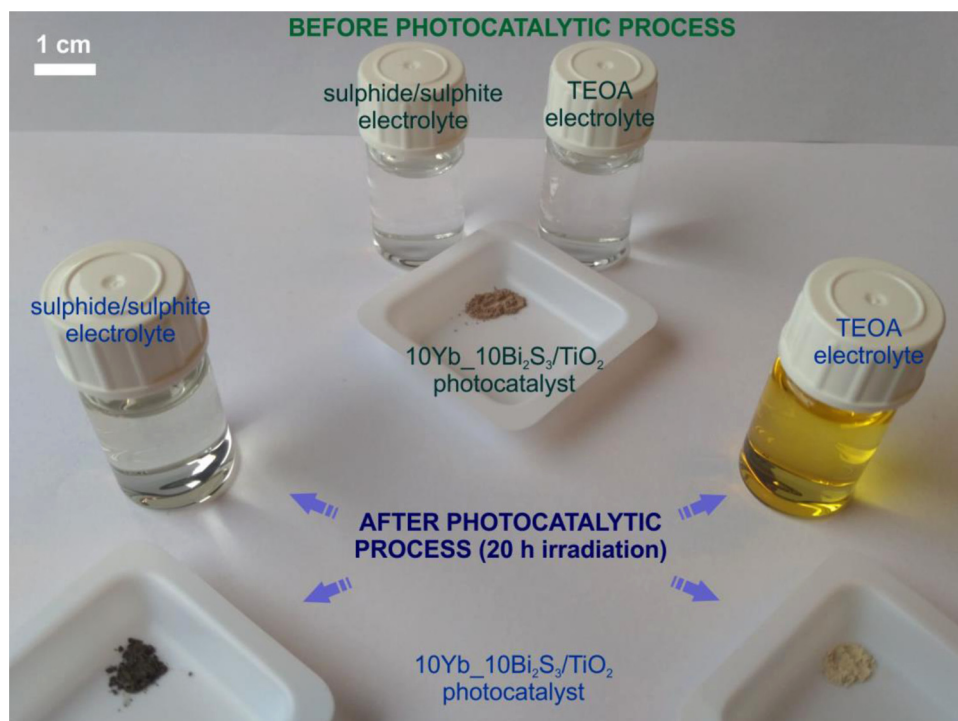
Fig. 11. Images of electrolytes and photocatalysts before and after prolonged (20-h) photocatalytic hydrogen generation.

located on the RE_{int} site, as displayed in Fig. 14a. Fig. 15 displays the electronic structure computed for RE_S, RE_{Bi}, and RE_{int}. The calculations yielded Er_S and Er_{int} with a Fermi level within the CB, while Yb_S and Yb_{int} showed a defective level within the BG with S 2p + Bi 6p character. Finally, Er_{Bi} and Yb_{Bi} had a hole defect state at the VB. Considering the results for RE occupying S sites, Bi sites, and interstitials, our SCAN + rVV10 calculations suggested that for Er, the most likely defect site location is Er_{Bi} with a formation energy of -6.40 eV (Table 5). In the case of Yb, Yb_{int} is the most likely site with a formation energy of -3.45 eV (Table 5). The electronic structures computed for the most stable defect location of Er (Er_{Bi}) and Yb (Yb_{int}) are displayed in Fig. 16. The computed PDOS show that $Er_{Bi}\_Bi_2S_3$ QDs have a BG of 1.4 eV, while the BG of $Yb_{int}\_Bi_2S_3$ QDs equals 0.4 eV.

The computed PDOS for Er_{Bi} show no defective level within the BG, while Yb_{int} presents a defect level with S 2p + Bi 6p character within the BG (Fig. 16). The electronic structures computed for other cases yield Er_S and Er_{int} with the Fermi level within the CB. Yb_S and Yb_{int} show a defect level with S 2p + Bi 6p character within the BG. Finally, Er_{Bi} and Yb_{Bi} have a hole defect state at the VB (cf. Fig. 15). Doping with Yb_{int} and Er_{int} was calculated to decrease the BG from 1.4 (1.98) to 0.4 and 0.7 eV, respectively. Interestingly, the RE_S defective site in RE-Bi_2S_3 QDs also decreased the BG, while the RE_{Bi} defective site had no

significant influence on the BG (Table 5).

3.7. Mechanism of photocatalytic reaction

Based on experimental and theoretical studies as well as on literature data [92,93], we proposed a mechanism for photocatalytic
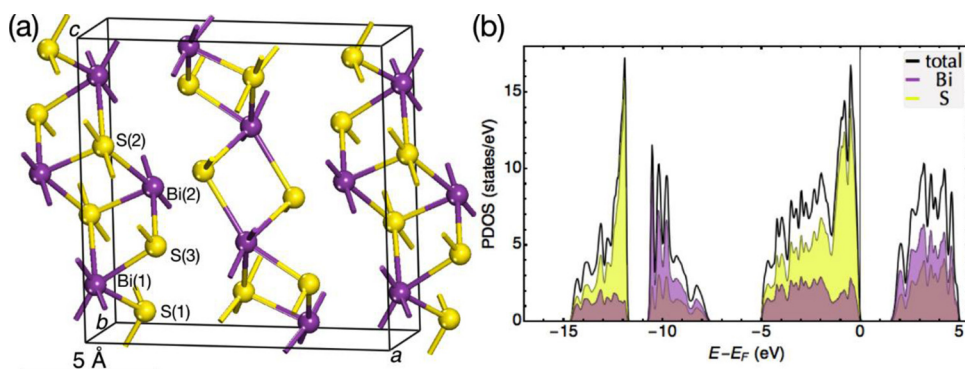
Table 4

Crystallographic data and physical properties of pristine Bi_2S_3 computed by SCAN + rVV10. The values correspond to those of the predicted unit cell, with u, v and w being fractional coordinates. The atomic sites correspond to those in Fig. 12. The E_g value in parentheses is the one predicted by HSE12.

Property	Calculated (SCAN + rVV10)	Sites	u	v	w
Space group	*Pbnm*	Bi(1)	0.0128	0.2500	0.1735
a(Å)	11.366	Bi(2)	0.1598	0.7500	0.4654
b(Å)	3.985	S(1)	0.1223	0.7500	0.0569
c(Å)	11.103	S(2)	0.0505	0.2500	0.6297
$\alpha = \beta = \gamma$ (°)	90	S(3)	0.2147	0.2500	0.3059
Volume (Å^3)	502.91				
B_0 (GPa)	34.0				
E_g (eV)	1.4 (1.98)				

Fig. 12. (Colour online) (a) Crystal structure of pristine Bi_2S_3 (*Pbnm* space group), with Bi (S) atoms represented by violet (yellow) spheres and the black line box outlining the unit cell. The S and Bi sites are labelled according to Table 4. (b) Partial density of states of pristine Bi_2S_3 computed by SCAN + rVV10. (For interpretation of the references to colour in this figure legend, the reader is referred to the web version of this article.)
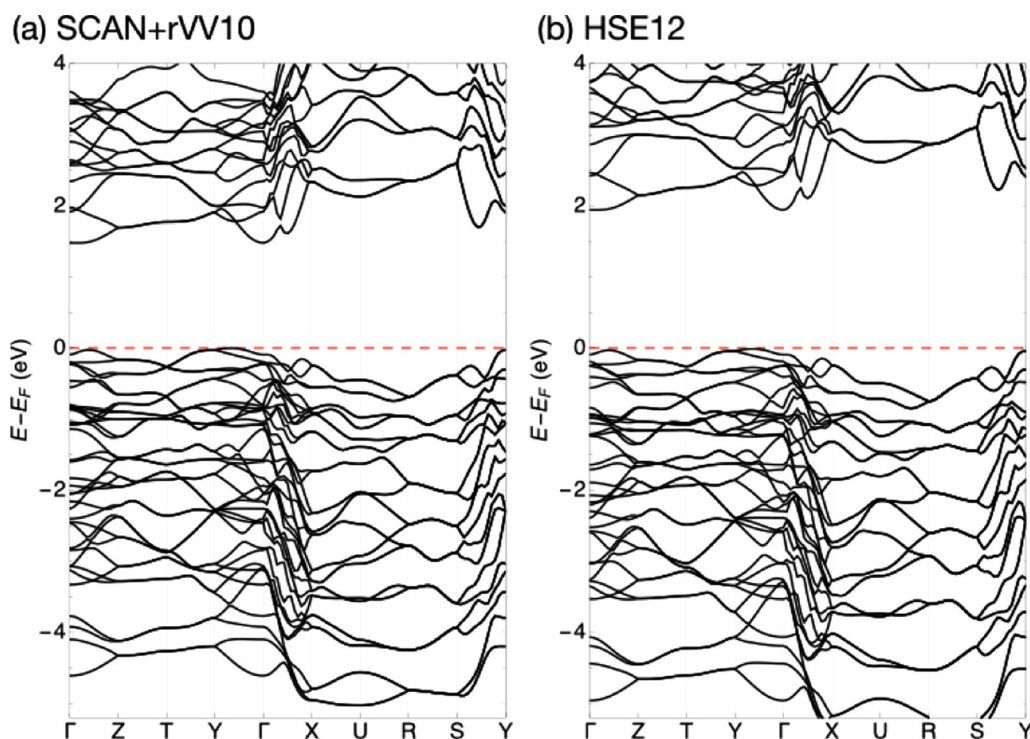
Fig. 13. Band structure of the pristine crystal structure of Bi_2S_3 computed using (a) SCAN + rVV10 (BG = 1.40 eV) and (b) HSE12 (BG = 1.98 eV). The results indicate the presence of an indirect BG.
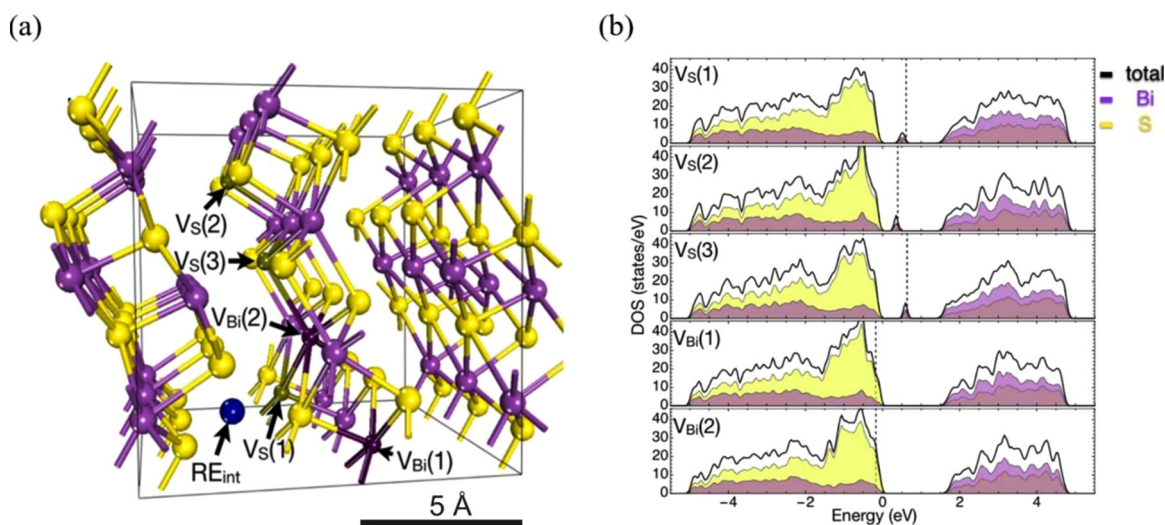

Fig. 14. (a) Bi_2S_3 (1 × 3 × 1) supercell with the location of defect sites as presented in Table 5, with violet (dark-violet) and yellow (dark-yellow) spheres representing Bi (V_{Bi}) and S (V_S) atoms (sites), respectively, and the dark-blue sphere showing the position of the RE interstitial. (b) SCAN + rVV10-computed PDOS for a (1 × 3 × 1) Bi_2S_3 supercell with V_S and V_{Bi} sites. The Fermi level is indicated by a vertical dotted line. (For interpretation of the references to colour in this figure legend, the reader is referred to the web version of this article.)

Table 5

SCAN + rVV10-computed formation energies (E_{for}) and BGs (E_g) [both in eV] for neutral defects: S and Bi vacancies (V_S and V_{Bi}, respectively). RE doping on S and Bi sites (RE_S and RE_{Bi}) and RE interstitials, RE_{int} with RE = Er and Yb. Defect labelling is in accordance with Fig. 14a.

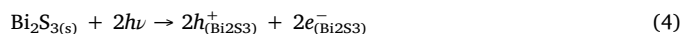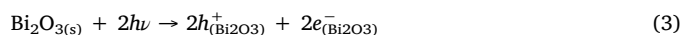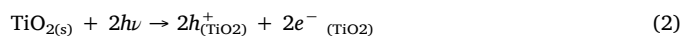|	V_S			V_{Bi}		RE_S		RE_{Bi}		RE_{int}	
	1	2	3	1	2	Er	Yb	Er	Yb	Er	Yb
E_{for}	4.84	4.78	4.66	7.53	7.36	−1.65	0.79	−6.40	−2.10	−5.73	−3.45
E_F	BG	BG	BG	VB	VB	CB	GB	VB	VB	CB	BG
E_g	0.8	0.9	0.7	1.4	1.4	0.7	0.4	1.4	1.5	0.7	0.4
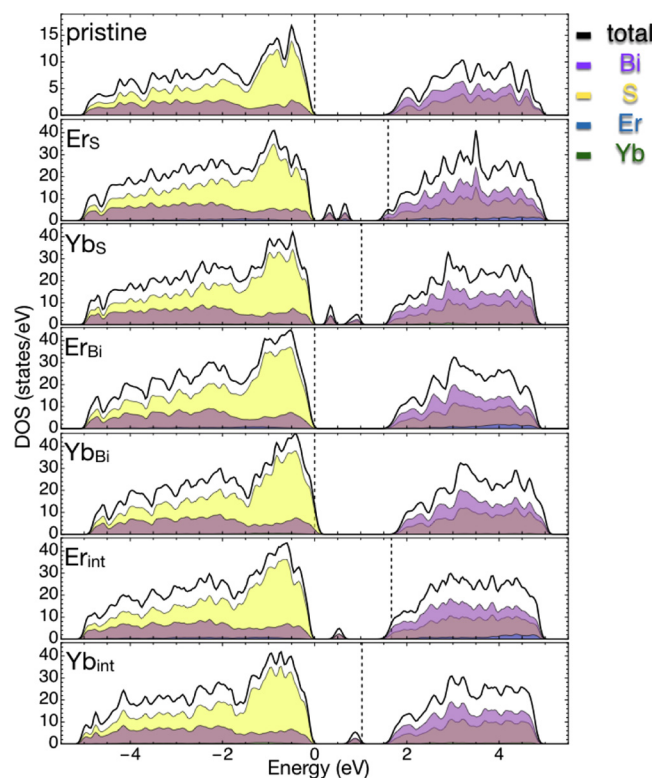
Fig. 15. (Colour online) SCAN + rVV10-computed PDOS for the $(1 \times 3 \times 1)$ Bi_2S_3 supercell with RE_S, RE_{Bi}, and RE_{int} defects. The Fermi level is located along the dotted line.

hydrogen generation over the most active photocatalyst, $10Yb\_10Bi_2S_3/TiO_2$ (Fig. 17). In line with the results of XPS analysis, which showed the presence of TiO_2 as well as Bi_2O_3 and Bi_2S_3 together with electronic states identifying the presence of Yb, the proposed mechanism involves interactions between the three semiconductors (TiO_2, Bi_2O_3, and Bi_2S_3 doped with Yb^{3+}).

As sulphides are known to be unstable during photocatalytic reactions [94,95] because of photocorrosion, Bi_2S_3 was also expected to show instability. Photocatalyst excitation affords electron-hole pairs, with electrons involved in the reduction of water to molecular hydrogen and the remaining holes involved in the oxidation of the sulphur-based photocatalyst (reaction (1)). Similarly to the case of CdS [87], Bi ions can be released into the solution upon the concomitant precipitation of elemental S to rapidly decrease catalyst activity and hydrogen yield.
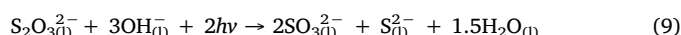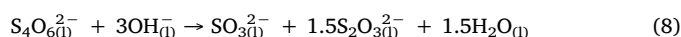
$$Bi_2S_{3(s)} + 6h^+ \rightarrow 2Bi_{(l)}^{3+} + 3S_{(s)} \tag{1}$$
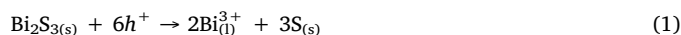
Sulphide photocorrosion can be inhibited through the use of a suitable sacrificial agent [87,96,97], as described in in our investigations. In the case of sulphides, sulphur-based electrolytes containing Na_2S, Na_2SO_3, and NaOH are most often used [87,97,98]. In these electrolytes, S^{2-} and SO_3^{2-} ions act as electron donors and participate in a series of reactions during the photocatalytic process to afford other sulphur-based ions such as S_2^{2-}, $S_2O_3^{2-}$, SO_4^{2-}, and $S_2O_6^{2-}$ [87,96]. During exposure to UV–vis light, the photocatalyst (TiO_2 as well as Bi_2O_3 and Bi_2S_3) is excited, which is followed by electron-hole generation in all involved semiconductors, as shown in reaction (2–4).

$$TiO_{2(s)} + 2h\nu \rightarrow 2h_{(TiO2)}^+ + 2e^-_{(TiO2)} \tag{2}$$

$$Bi_2O_{3(s)} + 2h\nu \rightarrow 2h_{(Bi2O3)}^+ + 2e^-_{(Bi2O3)} \tag{3}$$

$$Bi_2S_{3(s)} + 2h\nu \rightarrow 2h_{(Bi2S3)}^+ + 2e^-_{(Bi2S3)} \tag{4}$$

Electrons from the TiO_2 CB can be transported to the lower-lying CB of Bi_2O_3, while holes from the TiO_2 VB can be directly involved in the oxidation of water to oxygen.

In turn, holes created in the Bi_2S_3 VB can take part in the oxidation of S^{2-} and SO_3^{2-} anions to $S_2O_3^{2-}$ ions (reaction (5)), which are subsequently oxidised to $S_4O_6^{2-}$ ions (reaction (6)) or reduced by electrons created in the Bi_2O_3 CB to S^{2-} + SO_3^{2-} anions (reaction (7)). Additionally, in an alkaline environment (NaOH), $S_4O_6^{2-}$ ions can decompose into SO_3^{2-} and $S_2O_3^{2-}$ (reaction (8)), while $S_2O_3^{2-}$ ions, under the influence of light and hydroxyl ions, generate SO_3^{2-} and S^{2-} (reaction (9)). These ions (see Fig. 17) can be oxidised by holes originating from the Bi_2S_3 VB to $S_2O_3^{2-}$ ions, and the entire reaction cycle is repeated.

$$SO_{3(l)}^{2-} + S_{(l)}^{2-} + 2h^+ \rightarrow S_2O_{3(l)}^{2-} \tag{5}$$

$$S_2O_{3(l)}^{2-} + 2h^+ \rightarrow S_4O_{6(l)}^{2-} \tag{6}$$

$$S_2O_{3(l)}^{2-} + 2e^- \rightarrow S_{(l)}^{2-} + SO_{3(l)}^{2-} \tag{7}$$

$$S_4O_{6(l)}^{2-} + 3OH_{(l)}^- \rightarrow SO_{3(l)}^{2-} + 1.5S_2O_{3(l)}^{2-} + 1.5H_2O_{(l)} \tag{8}$$

$$S_2O_{3(l)}^{2-} + 3OH_{(l)}^- + 2h\nu \rightarrow 2SO_{3(l)}^{2-} + S_{(l)}^{2-} + 1.5H_2O_{(l)} \tag{9}$$

In this way, the oxidising effect of holes on the sulphide photocatalyst is blocked, and high-energy electrons arising from the Bi_2S_3 CB can be directly involved in the reduction of water to molecular hydrogen (reaction (10)), considering that Bi_2S_3 has the highest potential to reduce water molecules. Furthermore, the presence of Bi_2S_3 crystal lattice defects in the form of Yb^{3+} ions facilitates photocatalyst excitation with lower-energy irradiation by narrowing the BG of Bi_2S_3, as also demonstrated by computer simulations (Fig. 16).
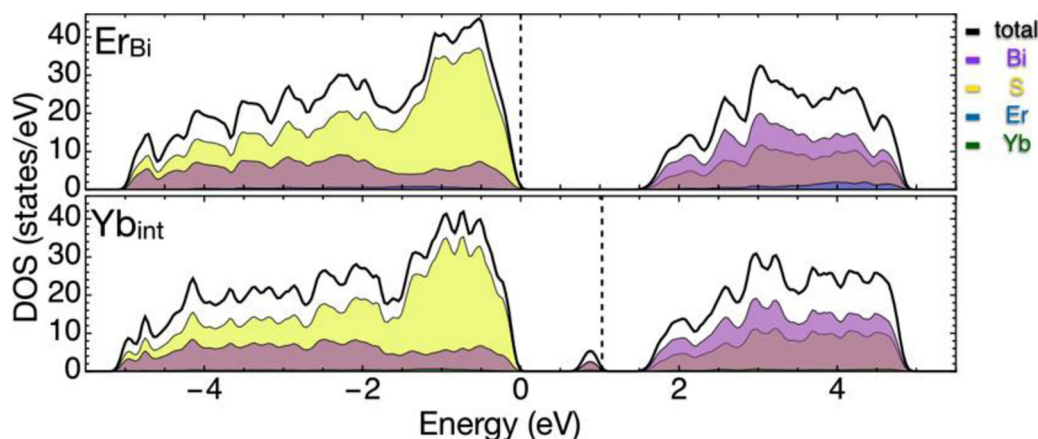

Fig. 16. (Colour online) SCAN + rVV10-computed PDOS for the most stable RE defects: Er_{Bi} and Yb_{int}, with dotted line indicating the position of the Fermi level.
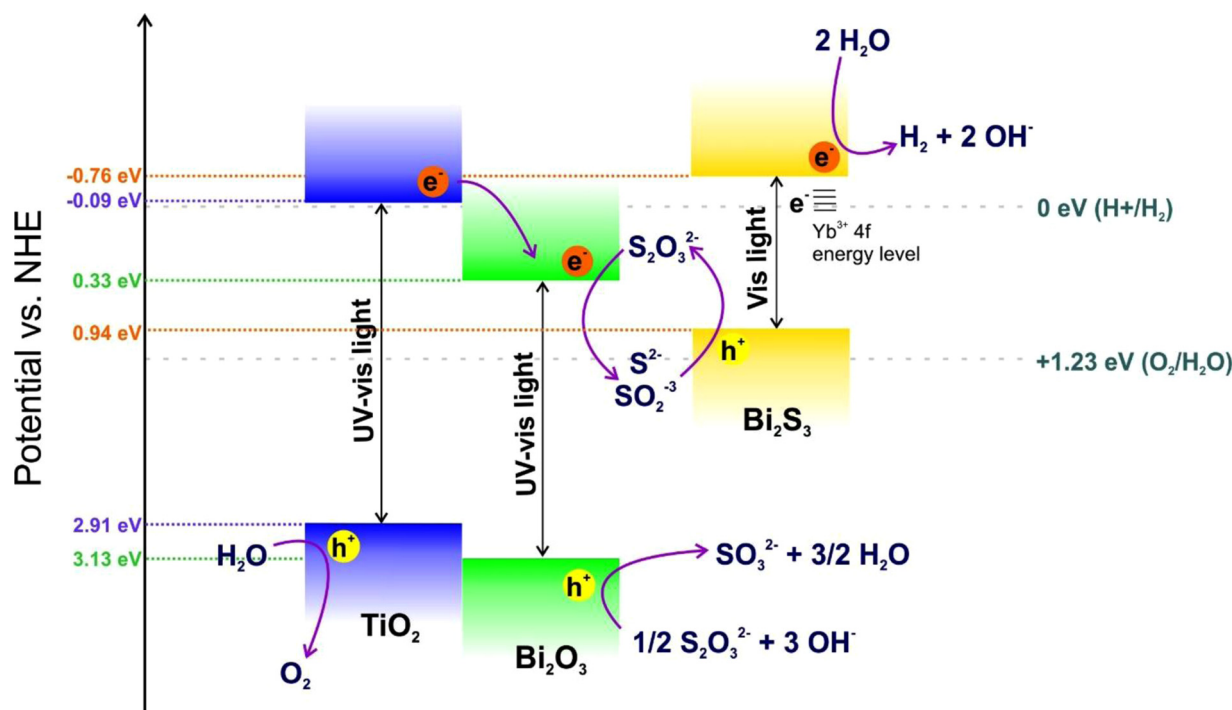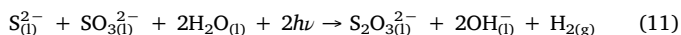
Fig. 17. Proposed mechanism of photocatalytic water splitting under UV–vis light in the presence of TiO_2 decorated by Yb-doped Bi_2O_3/Bi_2S_3 QDs.

$$2H_2O_{(l)} + h\nu \rightarrow H_{2(g)} + 2OH_{(l)}^- \qquad (10)$$

The large amount of hydrogen generated during the irradiation of the sulphur-based electrolyte in the absence of any photocatalyst can be explained by reaction (11).

$$S_{(l)}^{2-} + SO_{3(l)}^{2-} + 2H_2O_{(l)} + 2h\nu \rightarrow S_2O_{3(l)}^{2-} + 2OH_{(l)}^- + H_{2(g)} \qquad (11)$$

4. Conclusion

Photocatalysts including Bi_2S_3 and Er- or Yb-doped Bi_2S_3 QDs deposited on rutile TiO_2 spheres were prepared and characterised in terms of morphology and structural, surface, and optical properties. SEM and TEM imaging confirmed the presence of Bi_2S_3 and RE-Bi_2S_3 QDs (with diameters of 4–5 nm) evenly distributed on nanorod-comprising TiO_2 spheres with an expanded surface. UV–vis spectra confirmed the increase in the intensity of visible light absorption by TiO_2 after its decoration with pristine or doped Bi_2S_3 QDs. Moreover, photoluminescence spectroscopy revealed that compared to bare TiO_2, these hybrids featured a lower luminescence intensity. XPS analysis of the photocatalyst surface confirmed the presence of electron states due to Bi_2S_3 doped with Yb^{3+} and Er^{3+}, while XRD spectroscopy indicated the presence of only Bi_2O_3 and TiO_2 phases in composite samples. These findings demonstrated the partial oxidation of Bi_2S_3 and RE-doped Bi_2S_3 QDs on the TiO_2 surface during annealing at 300 °C in the last stage of the synthesis. As a result, the Bi_2O_3-Bi_2S_3-TiO_2 system composed of three semiconductors and doped with Yb or Er was constructed, and the action synergy of these components was observed for photocatalytic water decomposition to generate hydrogen under UV–vis and visible light. The highest photocatalytic activity was observed for $10Yb\_10Bi_2S_3/TiO_2$, both under UV–vis and visible light, with the corresponding rate constant of hydrogen evolution in a sulphur-based electrolyte oscillating at 94.1 and 0.24 µmol $g^{-1} h^{-1}$, respectively. The Na_2S/Na_2SO_3 electrolyte stabilised the photocatalyst during the photocatalytic process, in contrast to the 10 wt% TEOA electrolyte, which had a destructive effect on Bi_2S_3 QDs. To better understand the photocatalytic reaction mechanism and the structure of doped Bi_2S_3 QDs, a RE-Bi_2S_3 QDs model was constructed, and theoretical calculations were performed. As a result, it was proven that Er^{3+} and Yb^{3+} ions can be incorporated into the Bi_2S_3 structure, with the former ion preferentially occupying the sites of Bi atoms, and the latter ion preferring to be located in the interstitial space of the cell. This incorporation reduced the BGs of Er-Bi_2S_3 and Yb-Bi_2S_3 semiconductors, improved the transport of photogenerated charges during light exposure, and inhibited the recombination of these charges.

CRediT authorship contribution statement

Magdalena Miodyńska: Investigation, Methodology, Data curation, Writing - original draft, Writing - review & editing, Visualization. **Alicja Mikolajczyk:** Formal analysis, Software. **Beata Bajorowicz:** Project administration. **Julia Zwara:** Investigation. **Tomasz Klimczuk:** Investigation. **Wojciech Lisowski:** Investigation. **Grzegorz Trykowski:** Investigation. **Henry P. Pinto:** Formal analysis, Software. **Adriana Zaleska-Medynska:** Conceptualization, Supervision, Writing - review & editing, Project administration, Funding acquisition.

Declaration of Competing Interest

The authors declare that they have no known competing financial interests or personal relationships that could have appeared to influence the work reported in this paper.

Appendix A. Supplementary data

Supplementary data associated with this article can be found, in the online version, at https://doi.org/10.1016/j.apcatb.2020.118962.

References

[1] P. Zhang, T. Song, T. Wang, H. Zeng, Enhancement of hydrogen production of a Cu–TiO2 nanocomposite photocatalyst combined with broad spectrum absorption sensitizer Erythrosin B, RSC Adv. 7 (2017) 17873–17881, https://doi.org/10.1039/C6RA27686E.

[2] A. Zaleska-Medynska, Metal Oxide-Based Photocatalysis: Fundamentals and Prospects for Application, Elsevier, 2018.

[3] J. Huo, L. Fang, Y. Lei, G. Zeng, H. Zeng, Facile preparation of yttrium and aluminum co-doped ZnO via a sol–gel route for photocatalytic hydrogen production, J. Mater. Chem. A. 2 (2014) 11040–11044, https://doi.org/10.1039/C4TA02207F.

[4] H. Liu, K. Zhao, T. Wang, J. Deng, H. Zeng, Facile preparation of cerium (Ce) and antimony (Sb) codoped SnO2 for hydrogen production in lactic acid solution, Mater. Sci. Semicond. Process. 40 (2015) 670–675, https://doi.org/10.1016/j.mssp.2015.07.041.

[5] F. Raziq, M. Humayun, A. Ali, T. Wang, A. Khan, Q. Fu, W. Luo, H. Zeng, Z. Zheng, B. Khan, H. Shen, X. Zu, S. Li, L. Qiao, Synthesis of S-Doped porous g-C3N4 by using ionic liquids and subsequently coupled with Au-TiO2 for exceptional cocatalyst-free visible-light catalytic activities, Appl. Catal. B Environ. 237 (2018) 1082–1090, https://doi.org/10.1016/j.apcatb.2018.06.009.

[6] T. Song, P. Zhang, T. Wang, A. Ali, H. Zeng, Constructing a novel strategy for controllable synthesis of corrosion resistant Ti3 + self-doped titanium–silicon materials with efficient hydrogen evolution activity from simulated seawater, Nanoscale 10 (2018) 2275–2284, https://doi.org/10.1039/C7NR07095K.

[7] B. Bajorowicz, A. Gołąbiewska, J. Nadolna, A. Malankowska, M.P. Kobylański, A. Zaleska-Medynska, Quantum dot-decorated semiconductor micro- and nanoparticles: a review of their synthesis, characterization and application in photocatalysis, Adv. Colloid Interface Sci. 256 (2018) 352–372, https://doi.org/10.1016/j.cis.2018.02.003.

[8] J. Sowik, M. Miodyńska, B. Bajorowicz, A. Mikolajczyk, W. Lisowski, T. Klimczuk, D. Kaczor, A. Zaleska Medynska, A. Malankowska, Optical and photocatalytic properties of rare earth metal-modified ZnO quantum dots, Appl. Surf. Sci. 464 (2019) 651–663, https://doi.org/10.1016/j.apsusc.2018.09.104.

[9] M.C. Beard, A.G. Midgett, M.C. Hanna, J.M. Luther, B.K. Hughes, A.J. Nozik, Comparing multiple exciton generation in quantum dots to impact ionization in bulk semiconductors: implications for enhancement of solar energy conversion, Nano Lett. 10 (2010) 3019–3027, https://doi.org/10.1021/nl101490z.

[10] A.H. Reshak, Quantum dots in photocatalytic applications: efficiently enhancing visible light photocatalytic activity by integrating CdO quantum dots as sensitizers, Phys. Chem. Chem. Phys. 19 (2017) 24915–24927, https://doi.org/10.1039/C7CP05312F.

[11] L. Ge, F. Zuo, J. Liu, Q. Ma, C. Wang, D. Sun, L. Bartels, P. Feng, Synthesis and efficient visible light photocatalytic hydrogen evolution of polymeric g-C3N4 coupled with CdS quantum dots, J. Phys. Chem. C. 116 (2012) 13708–13714, https://doi.org/10.1021/jp3041692.

[12] C. Wang, R.L. Thompson, P. Ohodnicki, J. Baltrus, C. Matranga, Size-dependent photocatalytic reduction of CO2 with PbS quantum dot sensitized TiO2 heterostructured photocatalysts, J. Mater. Chem. 21 (2011) 13452–13457, https://doi.org/10.1039/C1JM12367J.

[13] G.-S. Li, D.-Q. Zhang, JC. Yu, A new visible-light photocatalyst: CdS quantum dots embedded mesoporous TiO2, Environ. Sci. Technol. 43 (2009) 7079–7085, https://doi.org/10.1021/es9011993.

[14] X. Wang, Z. Wang, M. Zhang, X. Jiang, Y. Wang, J. Lv, G. He, Z. Sun, Nanoheterostructure Engineering of CdS/PbS Quantum-Dot Co-Sensitized TiO 2 Nanorod Arrays for Enhanced Photoelectrochemical and Photocatalytic Properties, J. Electrochem. Soc. 164 (2017) H707–H713, https://doi.org/10.1149/2.0291712jes.

[15] B. Bajorowicz, J. Nadolna, W. Lisowski, T. Klimczuk, A. Zaleska-Medynska, The effects of bifunctional linker and reflux time on the surface properties and photocatalytic activity of CdTe quantum dots decorated KTaO 3 composite photocatalysts, Appl. Catal. B Environ. 203 (2017) 452–464, https://doi.org/10.1016/j.apcatb.2016.10.027.

[16] S. Azimi, A. Nezamzadeh-Ejhieh, Enhanced activity of clinoptilolite-supported hybridized PbS–CdS semiconductors for the photocatalytic degradation of a mixture of tetracycline and cephalexin aqueous solution, J. Mol. Catal. A Chem. 408 (2015) 152–160, https://doi.org/10.1016/j.molcata.2015.07.017.

[17] Y. Bessekhouad, D. Robert, J.V. Weber, Bi2S3/TiO2 and CdS/TiO2 heterojunctions as an available configuration for photocatalytic degradation of organic pollutant, J. Photochem. Photobiol. A Chem. 163 (2004) 569–580, https://doi.org/10.1016/j.jphotochem.2004.02.006.

[18] J. Fu, B. Chang, Y. Tian, F. Xi, X. Dong, Novel C3N4–CdS composite photocatalysts with organic–inorganic heterojunctions: in situ synthesis, exceptional activity, high stability and photocatalytic mechanism, J. Mater. Chem. A. 1 (2013) 3083–3090, https://doi.org/10.1039/C2TA00672C.

[19] T. Lv, L. Pan, X. Liu, T. Lu, G. Zhu, Z. Sun, C.Q. Sun, One-step synthesis of CdS–TiO2–chemically reduced graphene oxide composites via microwave-assisted reaction for visible-light photocatalytic degradation of methyl orange, Catal. Sci. Technol. 2 (2012) 754–758, https://doi.org/10.1039/C2CY00452F.

[20] W.-C. OH, M. CHEN, K. CHO, C. KIM, Z. MENG, L. ZHU, Synthesis of Graphene-CdSe composite by a simple hydrothermal method and its photocatalytic degradation of organic dyes, Chinese J. Catal. 32 (2011) 1577–1583, https://doi.org/10.1016/S1872-2067(10)60264-1.

[21] S.W. Cao, Y.P. Yuan, J. Fang, M.M. Shahjamali, F.Y.C. Boey, J. Barber, S.C. Joachim Loo, C. Xue, In-situ growth of CdS quantum dots on g-C3N4 nanosheets for highly efficient photocatalytic hydrogen generation under visible light irradiation, Int. J. Hydrogen Energy 38 (2013) 1258–1266, https://doi.org/10.1016/j.ijhydene.2012.10.116.

[22] R.M. Navarro, F. del Valle, J.L.G. Fierro, Photocatalytic hydrogen evolution from CdS–ZnO–CdO systems under visible light irradiation: Effect of thermal treatment and presence of Pt and Ru cocatalysts, Int. J. Hydrogen Energy 33 (2008) 4265–4273, https://doi.org/10.1016/j.ijhydene.2008.05.048.

[23] S.V. Kahane, R. Sasikala, B. Vishwanadh, V. Sudarsan, S. Mahamuni, CdO–CdS nanocomposites with enhanced photocatalytic activity for hydrogen generation from water, Int. J. Hydrogen Energy 38 (2013) 15012–15018, https://doi.org/10.1016/j.ijhydene.2013.09.077.

[24] X. Wang, G. Liu, G.Q. Lu, H.-M. Cheng, Stable photocatalytic hydrogen evolution from water over ZnO–CdS core–shell nanorods, Int. J. Hydrogen Energy 35 (2010) 8199–8205, https://doi.org/10.1016/j.ijhydene.2009.12.091.

[25] L. Xu, W. Shi, J. Guan, Preparation of crystallized mesoporous CdS/Ta2O5 composite assisted by silica reinforcement for visible light photocatalytic hydrogen evolution, Catal. Commun. 25 (2012) 54–58, https://doi.org/10.1016/j.catcom.2012.03.037.

[26] W. Cui, S. Ma, L. Liu, Y. Liang, PbS-sensitized K2Ti4O9 composite: preparation and photocatalytic properties for hydrogen evolution under visible light irradiation, Chem. Eng. J. 204–206 (2012) 1–7, https://doi.org/10.1016/j.cej.2012.07.075.

[27] M. Wang, J. Wang, S. Feng, P. Meng, Time-dependent toxicity of cadmium telluride quantum dots on liver and kidneys in mice: histopathological changes with elevated free cadmium ions and hydroxyl radicals, Int. J. Nanomedicine (2016) 2319–2328.

[28] R. Hardman, Review A Toxicologic Review of Quantum Dots: Toxicity Depends on Physicochemical and Environmental Factors, Environ. Health Perspect. 114 (2012) 165–172, https://doi.org/10.1289/ehp.8284.

[29] H. Zhang, H. Huang, H. Ming, H. Li, L. Zhang, Y. Liu, Z. Kang, Carbon quantum dots/Ag3PO4 complex photocatalysts with enhanced photocatalytic activity and stability under visible light, J. Mater. Chem. 22 (2012) 10501–10506, https://doi.org/10.1039/C2JM30703K.

[30] H. Yu, Y. Zhao, C. Zhou, L. Shang, Y. Peng, Y. Cao, L.-Z. Wu, C.-H. Tung, T. Zhang, Carbon quantum dots/TiO2 composites for efficient photocatalytic hydrogen evolution, J. Mater. Chem. A. 2 (2014) 3344–3351, https://doi.org/10.1039/C3TA14108J.

[31] H. Li, R. Liu, S. Lian, Y. Liu, H. Huang, Z. Kang, Near-infrared light controlled photocatalytic activity of carbon quantum dots for highly selective oxidation reaction, Nanoscale. 5 (2013) 3289–3297, https://doi.org/10.1039/C3NR00092C.

[32] X. Qian, D. Yue, Z. Tian, M. Reng, Y. Zhu, M. Kan, T. Zhang, Y. Zhao, Carbon quantum dots decorated Bi2WO6 nanocomposite with enhanced photocatalytic oxidation activity for VOCs, Appl. Catal. B Environ. 193 (2016) 16–21, https://doi.org/10.1016/j.apcatb.2016.04.009.

[33] D. Wang, L. Guo, Y. Zhen, L. Yue, G. Xue, F. Fu, AgBr quantum dots decorated mesoporous Bi2WO6 architectures with enhanced photocatalytic activities for methylene blue, J. Mater. Chem. A. 2 (2014) 11716–11727, https://doi.org/10.1039/C4TA01444H.

[34] Q. Chen, R. Tong, X. Chen, Y. Xue, Z. Xie, Q. Kuang, L. Zheng, Ultrafine ZnO quantum dot-modified TiO2 composite photocatalysts: the role of the quantum size effect in heterojunction-enhanced photocatalytic hydrogen evolution, Catal. Sci. Technol. 8 (2018) 1296–1303, https://doi.org/10.1039/C7CY02310C.

[35] D. Qu, M. Zheng, P. Du, Y. Zhou, L. Zhang, D. Li, H. Tan, Z. Zhao, Z. Xie, Z. Sun, Highly luminescent S, N co-doped graphene quantum dots with broad visible absorption bands for visible light photocatalysts, Nanoscale 5 (2013) 12272–12277, https://doi.org/10.1039/C3NR04402E.

[36] Y.-J. Yuan, S. Yang, P. Wang, Y. Yang, Z. Li, D. Chen, Z.-T. Yu, Z.-G. Zou, Bandgap-tunable black phosphorus quantum dots: visible-light-active photocatalysts, Chem. Commun. 54 (2018) 960–963, https://doi.org/10.1039/C7CC08211H.

[37] I. Zns, S. Yu, X. Fan, X. Wang, J. Li, Q. Zhang, A. Xia, L. Wu, Y. Zhou, G.R. Patzke, S. Wei, Ef fi cient photocatalytic hydrogen evolution with, Nat. Commun. (n.d.) 1–10. doi:10.1038/s41467-018-06294-y.

[38] J. Sun, L. Duan, Q. Wu, W. Yao, Synthesis of MoS2 quantum dots cocatalysts and their efficient photocatalytic performance for hydrogen evolution, Chem. Eng. J. 332 (2018) 449–455, https://doi.org/10.1016/j.cej.2017.09.026.

[39] Y.-J. Yuan, G. Fang, D. Chen, Y. Huang, L.-X. Yang, D.-P. Cao, J. Wang, Z.-T. Yu, Z.-G. Zou, High light harvesting efficiency CuInS2 quantum dots/TiO2/MoS2 photocatalysts for enhanced visible light photocatalytic H2 production, Dalton Trans. 47 (2018) 5652–5659, https://doi.org/10.1039/C8DT00356D.

[40] T.-L. Li, C.-D. Cai, T.-F. Yeh, H. Teng, Capped CuInS2 quantum dots for H2 evolution from water under visible light illumination, J. Alloys. Compd. 550 (2013) 326–330, https://doi.org/10.1016/j.jallcom.2012.10.157.

[41] V. Ramasamy, V. Mohana, V. Rajendran, Characterization of Ca doped CeO2 quantum dots and their applications in photocatalytic degradation, OpenNano. 3 (2018) 38–47, https://doi.org/10.1016/j.onano.2018.04.002.

[42] R. Sumi, A.R. Warrier, C. Vijayan, Visible-light driven photocatalytic activity of β -indium sulfide (In 2 S 3) quantum dots embedded in Nafion matrix, Physica E: Low-dimensional Systems and Nanostructures 105103 (n.d.). doi:10.1088/0022-3727/47/10/105103.

[43] N.L. Reddy, S. Emin, V.D. Kumari, S. Muthukonda Venkatakrishnan, CuO quantum dots decorated TiO2 nanocomposite photocatalyst for stable hydrogen generation, Ind. Eng. Chem. Res. 57 (2018) 568–577, https://doi.org/10.1021/acs.iecr.7b03785.

[44] M. Miodyńska, B. Bajorowicz, P. Mazierski, W. Lisowski, T. Klimczuk, M.J. Winiarski, A. Zaleska-Medynska, J. Nadolna, Preparation and photocatalytic properties of BaZrO3 and SrZrO3 modified with Cu2O/Bi2O3 quantum dots, Solid State Sci. 74 (2017) 13–23, https://doi.org/10.1016/j.solidstatesciences.2017.10.003.

[45] X. Lin, X. Guo, W. Shi, F. Guo, H. Zhai, Y. Yan, Q. Wang, Ag3PO4 quantum dots

sensitized AgVO3 nanowires: A novel Ag3PO4/AgVO3 nanojunction with enhanced visible-light photocatalytic activity, Catal. Commun. 66 (2015) 67–72, https://doi.org/10.1016/j.catcom.2015.03.015.

[46] W. Chen, T.-Y. Liu, T. Huang, X.-H. Liu, J.-W. Zhu, G.-R. Duan, X.-J. Yang, In situ fabrication of novel Z-scheme Bi2WO6 quantum dots/g-C3N4 ultrathin nanosheets heterostructures with improved photocatalytic activity, Appl. Surf. Sci. 355 (2015) 379–387, https://doi.org/10.1016/j.apsusc.2015.07.111.

[47] B. Li, Z. Cao, S. Wang, Q. Wei, Z. Shen, BiVO4 quantum dot-decorated BiPO4 nanorods 0D/1D heterojunction for enhanced visible-light-driven photocatalysis, Dalton Trans. 47 (2018) 10288–10298, https://doi.org/10.1039/C8DT02402B.

[48] A.P. Chowdhury, B.H. Shambharkar, S.G. Ghugal, S.S. Umare, A.G. Shende, Ethylene glycol mediated synthesis of SnS quantum dots and their application towards degradation of eosin yellow and brilliant green dyes under solar irradiation, RSC Adv. 6 (2016) 108290–108297, https://doi.org/10.1039/C6RA10532G.

[49] W. Zhao, Z. Wei, L. Ma, J. Liang, X. Zhang, Ag 2 S quantum dots based on flower-like SnS 2 as matrix and enhanced photocatalytic degradation, Materials (2019) 1–11, https://doi.org/10.3390/ma12040582.

[50] B. Bajorowicz, E. Kowalska, J. Nadolna, Z. Wei, M. Endo, B. Ohtani, A. Zaleska-Medynska, Preparation of CdS and Bi2S3 quantum dots co-decorated perovskite-type KNbO3 ternary heterostructure with improved visible light photocatalytic activity and stability for phenol degradation, Dalton Trans. 47 (2018) 15232–15245, https://doi.org/10.1039/C8DT03094D.

[51] S.R. Kadam, R.P. Panmand, R.S. Sonawane, S.W. Gosavi, B.B. Kale, A stable Bi2S3 quantum dot–glass nanosystem: size tuneable photocatalytic hydrogen production under solar light, RSC Adv. 5 (2015) 58485–58490, https://doi.org/10.1039/C5RA10244H.

[52] M. Bernechea, Y. Cao, G. Konstantatos, Size and bandgap tunability in Bi2S3 colloidal nanocrystals and its effect in solution processed solar cells, J. Mater. Chem. A. 3 (2015) 20642–20648, https://doi.org/10.1039/C5TA04441C.

[53] P. Mazierski, A. Mikolajczyk, B. Bajorowicz, A. Malankowska, A. Zaleska-medynska, J. Nadolna, Appl. Catal. B Environ. 233 (2018) 301–317, https://doi.org/10.1016/j.apcatb.2018.04.019.

[54] S. Obregón, A. Kubacka, M. Fernández-García, G. Colón, High-performance Er3+–TiO2 system: dual up-conversion and electronic role of the lanthanide, J. Catal. 299 (2013) 298–306, https://doi.org/10.1016/j.jcat.2012.12.021.

[55] W. Yang, X. Li, D. Chi, H. Zhang, Lanthanide-doped upconversion materials : emerging applications for photovoltaics and photocatalysis, Nanotechnology 482001 (n.d.). doi:10.1088/0957-4484/25/48/482001.

[56] J. Reszczyńska, T. Grzyb, J.W. Sobczak, W. Lisowski, M. Gazda, B. Ohtani, A. Zaleska, Lanthanide co-doped TiO2: the effect of metal type and amount on surface properties and photocatalytic activity, Appl. Surf. Sci. 307 (2014) 333–345, https://doi.org/10.1016/j.apsusc.2014.03.199.

[57] J. Reszczyńska, T. Grzyb, J.W. Sobczak, W. Lisowski, M. Gazda, B. Ohtani, A. Zaleska, Visible light activity of rare earth metal doped (Er3+, Yb3+ or Er3+/Yb3+) titania photocatalysts, Appl. Catal. B Environ. 163 (2015) 40–49, https://doi.org/10.1016/j.apcatb.2014.07.010.

[58] J. Reszczyńska, T. Grzyb, Z. Wei, M. Klein, E. Kowalska, B. Ohtani, A. Zaleska-Medynska, Photocatalytic activity and luminescence properties of RE3+–TiO2 nanocrystals prepared by sol–gel and hydrothermal methods, Appl. Catal. B Environ. 181 (2016) 825–837, https://doi.org/10.1016/j.apcatb.2015.09.001.

[59] P. Mazierski, W. Lisowski, T. Grzyb, M.J. Winiarski, T. Klimczuk, A. Mikołajczyk, J. Flisikowski, A. Hirsch, A. Kołakowska, T. Puzyn, A. Zaleska-medynska, J. Nadolna, Enhanced photocatalytic properties of lanthanide-TiO2 nanotubes: an experimental and theoretical study, Appl. Catal. B, Environ. (2016), https://doi.org/10.1016/j.apcatb.2016.12.044.

[60] X. Wang, D. Li, Y. Guo, X. Wang, Y. Du, R. Sun, Preparation of lanthanide doped CdS, ZnS quantum dots in natural polysaccharide template and their optical properties, Opt. Mater. (Amst) 34 (2012) 646–651, https://doi.org/10.1016/j.optmat.2011.09.013.

[61] A. Sarkar, A.B. Ghosh, N. Saha, A.K. Dutta, D.N. Srivastava, P. Paul, B. Adhikary, Enhanced photocatalytic activity of Eu-doped Bi2S3 nanoflowers for degradation of organic pollutants under visible light illumination, Catal. Sci. Technol. 5 (2015) 4055–4063, https://doi.org/10.1039/C5CY00473J.

[62] Y. Xue, J. Lin, Y. Fan, A. Elsanousi, X. Xu, J. Mi, J. Li, X. Zhang, Y. Lu, T. Zhang, C. Tang, Controllable synthesis of uniformly distributed hollow rutile TiO 2 hierarchical microspheres and their improved photocatalysis, Mater. Chem. Phys. 143 (2013) 446–454, https://doi.org/10.1016/j.matchemphys.2013.09.026.

[63] Y. Wang, F. Xin, J. Chen, T. Xiang, X. Yin, Photocatalytic reduction of CO 2 in Isopropanol on exposed 001 facets, J. Nanosci. Nanotechnol. 17 (2017) 1863–1869, https://doi.org/10.1166/jnn.2017.12871.

[64] G. Kresse, J. Furthmüller, Efficient iterative schemes for ab initio total-energy calculations using a plane-wave basis set, Phys. Rev. B 54 (1996) 11169–11186, https://doi.org/10.1103/PhysRevB.54.11169.

[65] G. Kresse, J. Furthmüller, Efficiency of ab-initio total energy calculations for metals and semiconductors using a plane-wave basis set, Comput. Mater. Sci. 6 (1996) 15–50, https://doi.org/10.1016/0927-0256(96)00008-0.

[66] G. Kresse, D. Joubert, From ultrasoft pseudopotentials to the projector augmented-wave method, Phys. Rev. B 59 (1999) 1758–1775, https://doi.org/10.1103/PhysRevB.59.1758.

[67] J. Sun, A. Ruzsinszky, J.P. Perdew, Strongly Constrained and Appropriately Normed Semilocal Density Functional, Phys. Rev. Lett. 115 (2015) 36402, https://doi.org/10.1103/PhysRevLett.115.036402.

[68] J. Sun, R.C. Remsing, Y. Zhang, Z. Sun, A. Ruzsinszky, H. Peng, Z. Yang, A. Paul, U. Waghmare, X. Wu, M.L. Klein, J.P. Perdew, Accurate first-principles structures and energies of diversely bonded systems from an efficient density functional, Nat. Chem. 8 (2016) 831.

[69] H. Peng, Z.-H. Yang, J.P. Perdew, J. Sun, Versatile van der waals density functional based on a meta-generalized gradient approximation, Phys. Rev. X 6 (2016) 41005, https://doi.org/10.1103/PhysRevX.6.041005.

[70] J. Heyd, G.E. Scuseria, M. Ernzerhof, J. Heyd, G.E. Scuseria, M. Ernzerhof, Hybrid functionals based on a screened Coulomb potential Hybrid functionals based on a screened Coulomb potential, J. Chem. Phys. 8207 (2003), https://doi.org/10.1063/1.1564060.

[71] S.F. Wang, F. Gu, Z. Sen Yang, M.K. Lu, Facile synthesis of silica-coated Bi 2 S 3 nanorods and hollow silica nanotubes, J. Cryst. Growth 282 (2005) 79–84, https://doi.org/10.1016/j.jcrysgro.2005.04.082.

[72] M. Klein, J. Nadolna, A. Gołąbiewska, P. Mazierski, T. Klimczuk, H. Remita, A. Zaleska-Medynska, The effect of metal cluster deposition route on structure and photocatalytic activity of mono- and bimetallic nanoparticles supported on TiO2 by radiolytic method, Appl. Surf. Sci. 378 (2016) 37–48, https://doi.org/10.1016/j.apsusc.2016.03.191.

[73] P. Mazierski, M. Nischk, M. Gołkowska, W. Lisowski, M. Gazda, M.J. Winiarski, T. Klimczuk, A. Zaleska-Medynska, Photocatalytic activity of nitrogen doped TiO2 nanotubes prepared by anodic oxidation: the effect of applied voltage, anodization time and amount of nitrogen dopant, Appl. Catal. B Environ. 196 (2016) 77–88, https://doi.org/10.1016/j.apcatb.2016.05.006.

[74] H. Tang, H. Berger, P.E. Schmid, F. Lévy, Optical properties of anatase (TiO2), Solid State Commun. 92 (1994) 267–271, https://doi.org/10.1016/0038-1098(94)90889-3.

[75] F.J. Knorr, C.C. Mercado, J.L. McHale, Trap-State Distributions and Carrier Transport in Pure and Mixed-Phase TiO2: Influence of Contacting Solvent and Interphasial Electron Transfer, J. Phys. Chem. C. 112 (2008) 12786–12794, https://doi.org/10.1021/jp8039934.

[76] P.C, A. Naumkin, A. Kraut-Vass, S. Gaarenstroom, NIST X-ray photoelectron spectroscopy database 20, version 4.1, Natl. Inst. Stand. Technol. Gaithersbg. (2012), https://doi.org/10.18434/T4T88K.

[77] Y. Wang, Y. Wang, Y. Meng, H. Ding, Y. Shan, X. Zhao, X. Tang, A Highly Efficient Visible-Light-Activated Photocatalyst Based on Bismuth- and Sulfur-Codoped TiO2, J. Phys. Chem. C. 112 (2008) 6620–6626, https://doi.org/10.1021/jp7110007.

[78] G.T.K. Swami, F.E. Stageberg, A.M. Goldman, XPS characterization of erbium sesquioxide and erbium hydroxide, J. Vac. Sci. Technol. A 2 (1984) 767–770, https://doi.org/10.1116/1.572568.

[79] J. Zhou, L. Jiang, D. Chen, J. Liang, L. Qin, L. Bai, X. Sun, Y. Huang, Facile synthesis of Er-doped BiFeO3 nanoparticles for enhanced visible light photocatalytic degradation of tetracycline hydrochloride, J. Solgel Sci. Technol. 90 (2019) 535–546, https://doi.org/10.1007/s10971-019-04932-5.

[80] R.P. Panmand, M.V. Kulkarni, M. Valant, S.W. Gosavi, B.B. Kale, R.P. Panmand, M.V. Kulkarni, M. Valant, Quantum confinement of Bi2S3 in glass with magnetic behavior Quantum confinement of Bi 2 S 3 in glass with magnetic behavior, AIP Adv. 022123 (2013) 0–11, https://doi.org/10.1063/1.4794155.

[81] A.B. Kathare, Development of Bismuth Sulphide Quantum Dot' s in Silicate Glass Matrix, Int. J. Sci. Res. 6 (2017) 515–521.

[82] P.K. Panigrahi, A. Pathak, The growth of bismuth sulfide nanorods from spherical-shaped amorphous precursor particles under hydrothermal condition, J. Nanoparticles 2013 (2013) 1–12.

[83] T.A.F, A.S. Kanishcheva, Y.N. Mikhailov, Refinement of the crystal-structure of synthetic bismuthinite, Inorg. Mater. Appl. Res. 17 (1981) 1466–1468.

[84] The crystal structure of rutile as a function of temperature up to 1600° C, Zeitschrift für krist, Cryst. Mater. 194 (1991) 305, https://doi.org/10.1524/zkri.1991.194.14.305.

[85] O. Bi, Z. Jie, X. Ying, Assisted hydrothermal synthesis of Sb 2 S 3 and Bi 2 S 3 nanocrystals and their elevated-temperature oxidation behavior for conversion into, J. Phy. Chem. Solids Biomol. 70 (2009) 1121–1131, https://doi.org/10.1016/j.jpcs.2009.06.010.

[86] F. Liu, Y. Yang, J. Liu, W. Huang, Z. Li, Preparation of Bi 2 O 3 @ Bi 2 S 3 core – shell nanoparticle assembled thin films and their photoelectrochemical and photoresponsive properties, J. Electroanal. Chem. 665 (2012) 58–62, https://doi.org/10.1016/j.jelechem.2011.11.015.

[87] R.K. Chava, J.Y. Do, M. Kang, A. Abdel-wahab, Photocatalytic Hydrogen Production: Role of Sacrificial Reagents on the Activity of Oxide, Carbon, and Sulfide Catalysts, Catalysts (n.d.). doi:10.3390/catal9030276.

[88] Y. Huang, J. Qin, X. Liu, D. Wei, H. Jin, Hydrothermal synthesis of flower-like Na-doped α-Bi2O3 and improved photocatalytic activity via the induced oxygen vacancies, J. Taiwan Inst. Chem. Eng. (2018), https://doi.org/10.1016/j.jtice.2018.11.029.

[89] J. Zhang, Y. Wang, RSC Advances A convenient method to prepare a novel alkali metal sodium doped carbon nitride photocatalyst with a tunable band structure †, RSC Adv. 4 (2014) 62912–62919, https://doi.org/10.1039/C4RA11377B.

[90] L. Zhang, N. Ding, M. Hashimoto, K. Iwasaki, N. Chikamori, K. Nakata, Y. Xu, J. Shi, H. Wu, Y. Luo, D. Li, A. Fujishima, Q. Meng, Sodium-doped carbon nitride nanotubes for efficient visible light-driven hydrogen production, Nano Res. 11 (2018) 2295–2309, https://doi.org/10.1007/s12274-017-1853-3.

[91] X. Yu, C. Cao, H. Zhu, Synthesis and photoluminescence properties of Bi2S3 nanowires via surfactant micelle-template inducing reaction, Solid State Commun. 134 (2005) 239–243, https://doi.org/10.1016/j.ssc.2005.01.035.

[92] F.-A. Liu, Y.-C. Yang, J. Liu, W. Huang, Z.-L. Li, Preparation of Bi2O3@Bi2S3 core–shell nanoparticle assembled thin films and their photoelectrochemical and photoresponsive properties, J. Electroanal. Chem. 665 (2012) 58–62, https://doi.org/10.1016/j.jelechem.2011.11.015.

[93] D.Y.C. Leung, X. Fu, C. Wang, M. Ni, M.K.H. Leung, X. Wang, X. Fu, Hydrogen production over titania-based photocatalysts, ChemSusChem. 3 (2010) 681–694, https://doi.org/10.1002/cssc.201000014.

[94] Z. Shi, X. Dong, H. Dang, Facile fabrication of novel red phosphorus-CdS composite photocatalysts for H2 evolution under visible light irradiation, Int. J. Hydrogen Energy 41 (2016) 5908–5915, https://doi.org/10.1016/j.ijhydene.2016.02.146.

[95] C. Wang, L. Wang, J. Jin, J. Liu, Y. Li, M. Wu, L. Chen, B. Wang, X. Yang, B.-L. Su, Probing effective photocorrosion inhibition and highly improved photocatalytic hydrogen production on monodisperse PANI@CdS core-shell nanospheres, Appl. Catal. B Environ. 188 (2016) 351–359, https://doi.org/10.1016/j.apcatb.2016.02.017.

[96] M. Wang, S. Shen, Effects of sacrificial reagents on photocatalytic hydrogen evolution over different photocatalysts, J. Mater. Sci. (2017), https://doi.org/10.1007/s10853-017-0752-z.

[97] Y.G. Kim, W. Jo, ScienceDirect Photodeposited-metal / CdS / ZnO heterostructures for solar photocatalytic hydrogen production under different conditions, Int. J. Hydrogen Energy (2017) 1–8, https://doi.org/10.1016/j.ijhydene.2017.02.176.

[98] N. Bao, L. Shen, T. Takata, K. Domen, Self-templated synthesis of nanoporous CdS nanostructures for highly efficient photocatalytic hydrogen production under visible light, Chem. Mater. (2008) 110–117.